A Review of Aeronautical Fatigue Investigations in Sweden During the Period April 2021 to March 2023

Edited by: **Zlatan Kapidzic**
Saab AB
Sweden

Saab Doc. No: LN-070978
Date: 21 June 2023

Presented at the 38th Conference of the International Committee on Aeronautical Fatigue and Structural Integrity (ICAF), Delft, The Netherlands, 26-29 June 2023.

Contents

1 INTRODUCTION

In this paper a review is given of the work carried out in Sweden in the area of aeronautical fatigue and structural integrity during the period April 2021 to March 2023. The review includes basic studies and industrial applications.

Contributions to the present review are from the following instances:

- Saab AB
  Sections 2.1, 2.2, 2.3, 2.4, 3.1, 3.2, 3.3, 3.4, 3.5, 4.1, 4.5, 5.1

- Linköping University (LiU)
  Sections 3.4, 4.6, 5.1

- Mid Sweden University (MittU)
  Section 4.5, 4.6

- Bare AB
  Sections 4.2, 4.3, 4.4

- VTT (Technical Research Centre of Finland Ltd.)
  Section 2.2

- NewSoTech
  Section 5.1

2 FULL-SCALE FATIGUE AND DAMAGE TOLERANCE TESTING

2.1 Damage tolerance test verification programme for Gripen E/F airframe

Z. Kapidzic[1], *J-E. Lindbäck*[1]

[1]Saab Aeronautics, Linköping, Sweden

Background

Service life and damage tolerance capability of the airframe structure need to be verified by testing. The tests can either be based on similarities to previously conducted tests, if applicable, or by new tests when no previous test results are available. Full-scale testing is required when:

- Changed design principles in primary load paths
- Changed material in safety-of-flight critical parts
- Significant change of stress conditions in legacy primary load paths

When Gripen A/B was initially developed, the test verification task was huge since all of the above criteria applied. Especially the implementation of the damage tolerance task according to the MIL-A-83444 specification called for test verification. An extensive fatigue and damage tolerance test program of full-scale test assemblies was accomplished, see Fig. 2.1-1. Both airframe and systems parts, e.g. actuators in the flight control system, were included and a total of about 800 artificial defects, sizing between .05 and .25 inch, were introduced in the structural parts and in the correct structural surroundings. In addition conventional full-scale static and fatigue tests of both A and B versions were conducted covering testing beyond ultimate loads and 4 lifetimes respectively.

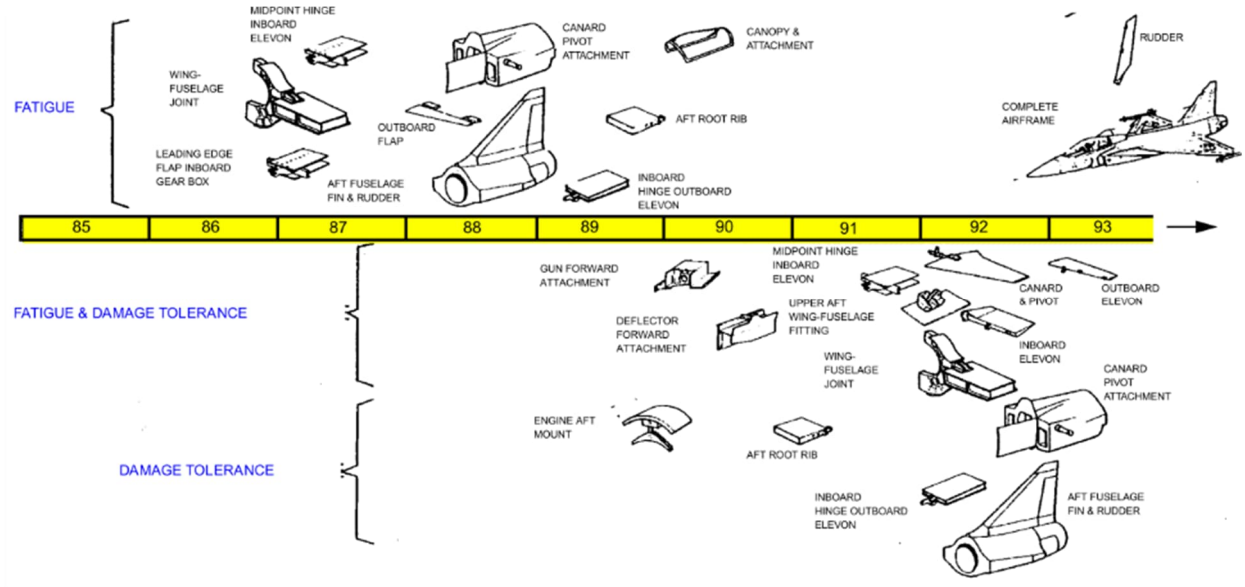

Figure 2.1-1. Test programme for fatigue and damage tolerance verification of Gripen A/B airframe.

When Gripen C/D was developed, no change of materials was done and no change of major load paths. Essential changes of local geometries were however done through the redesign to integral structures, extended service life (from 4,000 to 8,000 hours) and increased basic design mass (~10% compared to A/B versions) and some other load and structural changes, e.g. air-to-air refueling probe, called for new full-scale fatigue tests, se Fig. 2.1-2. Damage tolerance

tests were however not done in any large extent since the load path were the same although redesigned but the validation effort done on the fracture mechanic based damage tolerance methods during the A/B developments were deemed to be sufficient also for the C/D versions.

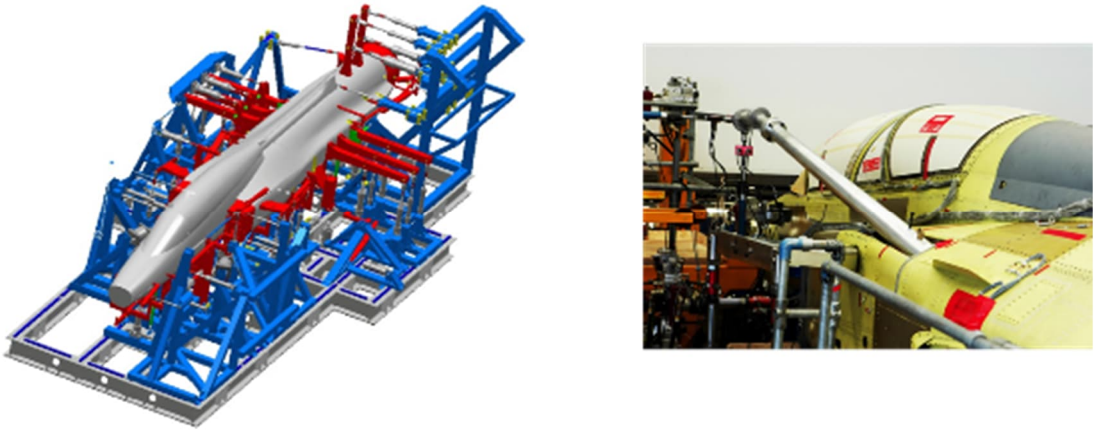

Figure 2.1-2. Full-scale fatigue test of Gripen D version.

With the development of Gripen NG versions E/F, structural changes were made that interrogated with several of the criteria for the need of test verification. Certification for airworthiness by full-scale testing is required due to:

- New mid fuselage/wing design, fuselage joints, MLG attachments
- Change of classification of parts due to design-for-manufacturing purposes
- Use of a new materials
- Increased basic design mass (~40% compared to C/D versions)
- New operational profiles

These structural changes call for a more extensive test programme than what was needed for the C/D versions. A full-scale static test (including impact damaged composite parts) of the complete airframe has been performed and two full-scale fatigue tests of the complete airframes of E and F versions are planned to be tested in the same rig for 4 lifetimes, see Fig. 2.1-3. In addition to the full-scale fatigue test, control surfaces (not included in the test airframe) will be tested in separate assemblies. These tests will be a combined fatigue and damage tolerance test by initially cycled for 2 lifetimes without artificial initial defect followed by 2 lifetimes with artificially manufactured defects installed.

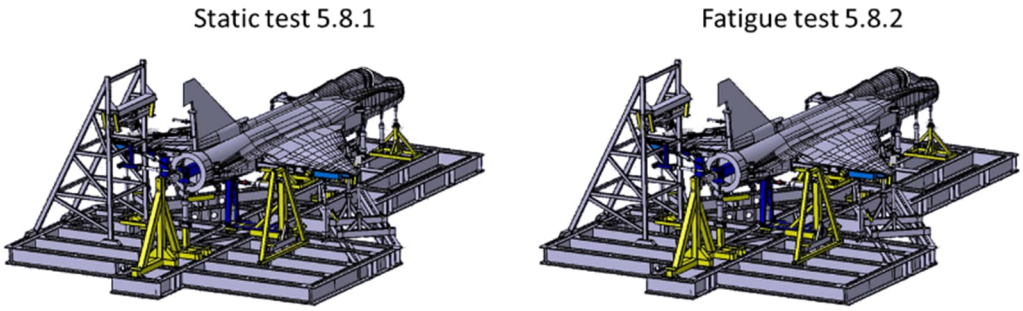

Figure 2.1-3. Full-scale fatigue tests of Gripen E version.

Full-scale tests of assemblies for compliance with damage tolerance requirements are also needed due to the structural changes in load paths and the upgraded classification of fuselage stringer joints and the design change of the wing to fuselage joint. To assure necessary and sufficient confidence regarding damage tolerance, a significant test effort designed to challenge

typical airframe crack scenarios with part through cracks (surface cracks in thickness steps, open and loaded holes etc.) was accomplished. Figure 2.1-4 shows structural objects/assemblies which are verified for damage tolerance when having multiple artificial initial defects installed in critical sections. The full-scale static test of Gripen E airframe and some of the completed tests of assemblages from Fig. 2.1-4 are described in more detail in the following sections.

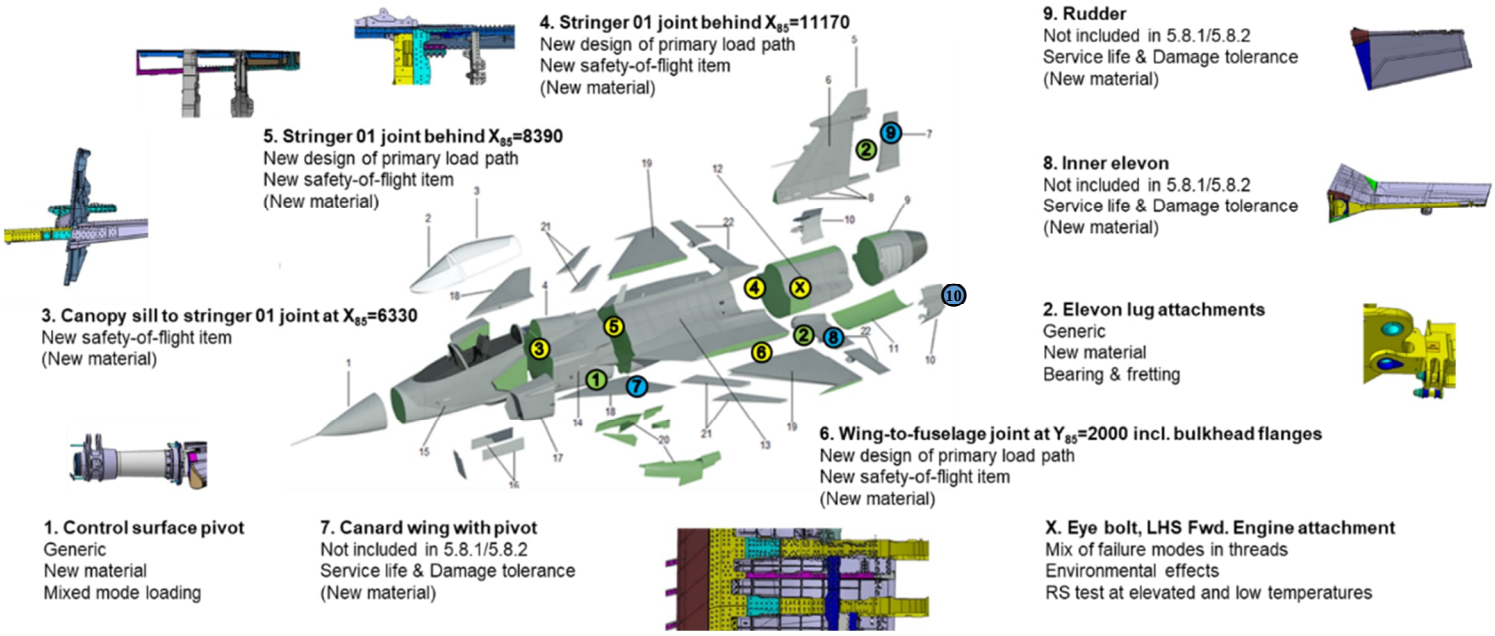

Figure 2.1-4. Full-scale damage tolerance tests of assemblies having artificial defects installed.

Full-scale static test of Gripen E airframe

A full-scale static test of the Gripen E single seater airframe, see Figure 2.1-5, has being successfully conducted and some details of the testing were outlined in [1]. The test objectives, to verify the static strength requirements and to verify the stiffness/load distribution in the global FE-model, have been achieved. Static strength of the fuselage has been verified for 150% LL and the strength of the wing, wing joints, fin and fin attachments have been verified for 180% LL. Also the strength of the attachments for the flaps, elevons, rudder, weapon pylons, radar, AAR, landing gears, canards, air intakes and the engine have been verified by testing. This means that the test aircraft can fly without restrictions on the airframe. Only some minor outcomes in the test have led to design updates for the serial version of Gripen E.

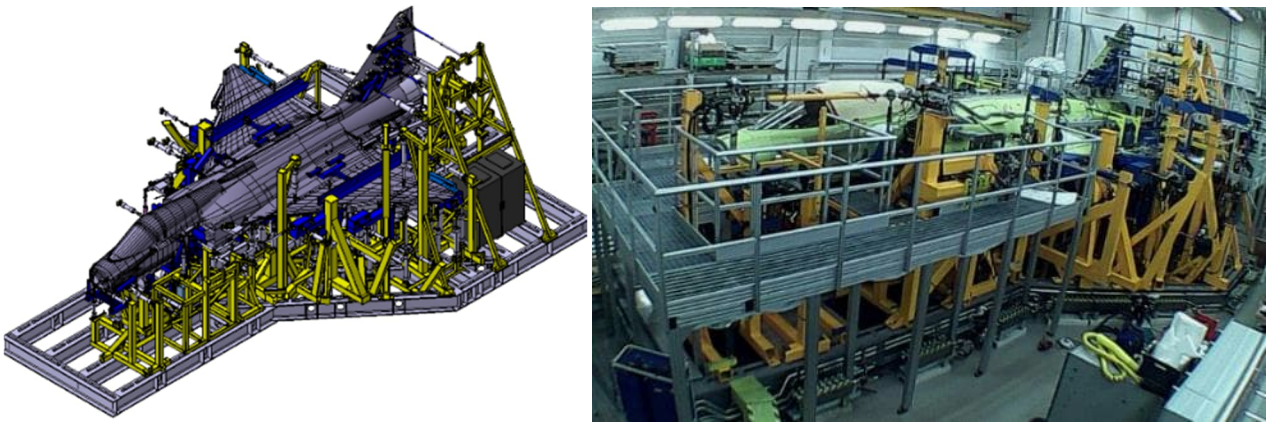

Figure 2.1-5. Static test set-up, Gripen E airframe.

Damage tolerance tests of assemblages of airframe components

Damage tolerance tests of assemblages: wing-to-fuselage joint (#6 in Fig. 2.1-4), canopy sill-to-stringer joint (#3 in Fig. 2.1-4), stringer joint at X_{85}=8390 (#5 in Fig. 2.1-4) and stringer joint at X_{85}=11770 (#4 in Fig. 2.1-4) are completed. Details regarding the test results can be found in [1] and [2] and Figures 2.1-6 to 9 show the test objects mounted in the rig.

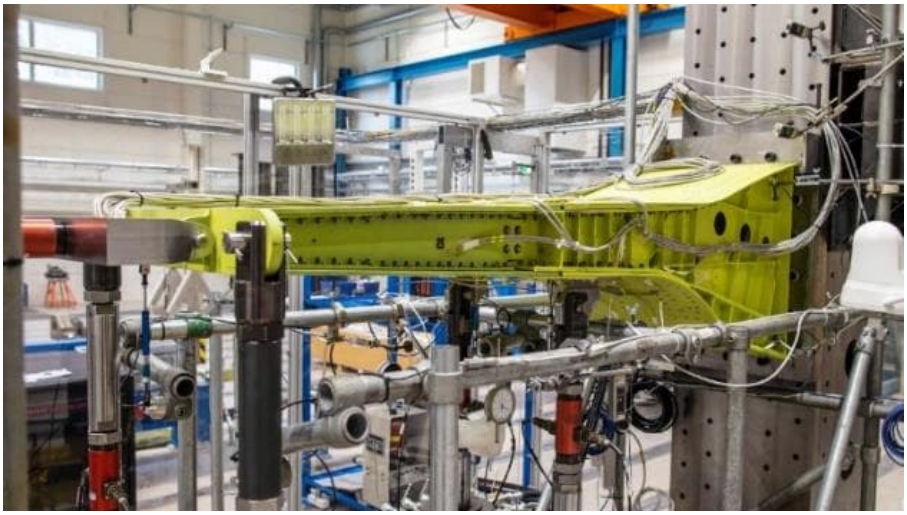

Figure 2.1-6. The test object and arrangement of the wing-to-fuselage joint test.

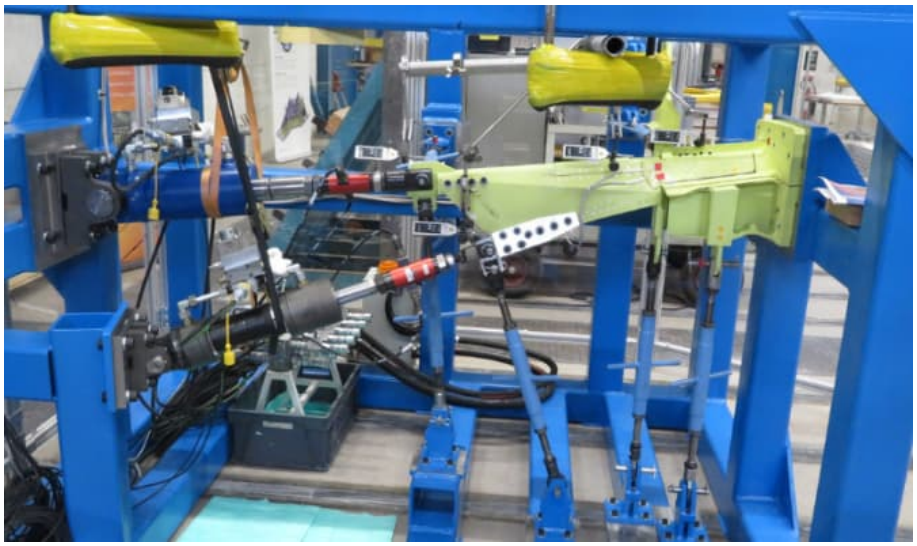

Figure 2.1-7. The test object and arrangement of the Gripen E canopy sill-to-stringer joint test.

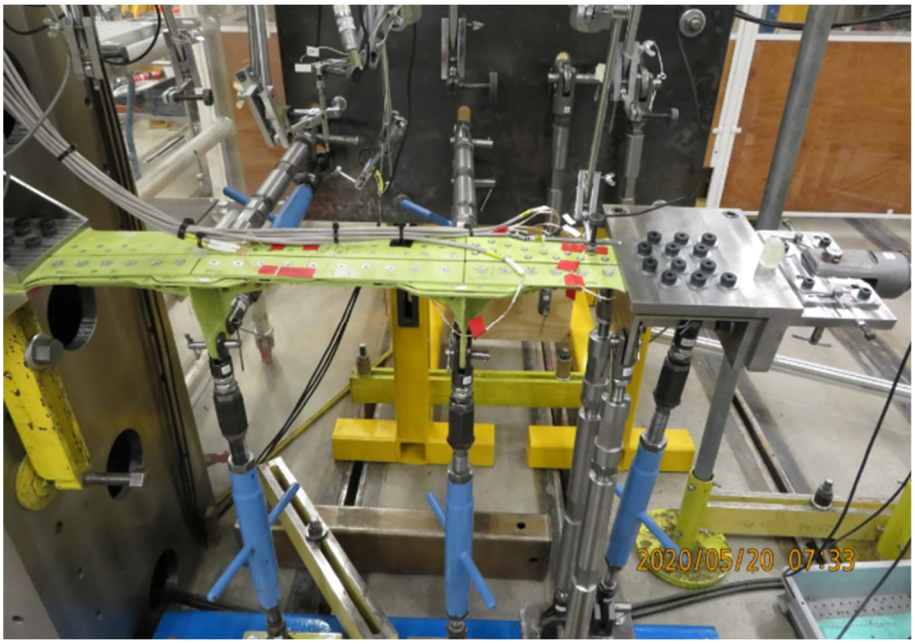

Figure 2.1-8. The test object and arrangement of the stringer joint test behind X_{85}=8390.

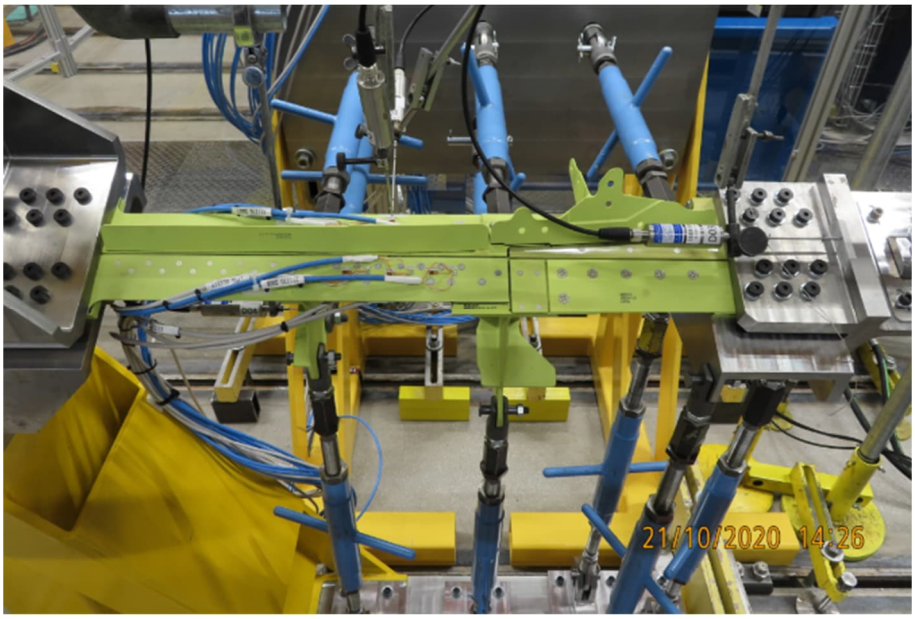

Figure 2.1-9. The test object and arrangement of the stringer joint test behind X_{85}=11770.

During last two years, fatigue and damage tolerance tests were performed on: canopy sill-to-stringer joint for F version (#3 in Fig. 2.1-4), air brake (#10 in Fig. 2.1-4), E/F rudder (#9 in Fig. 2.1-4) and the canard test (#7 in Fig. 2.1-4) is on-going. The E/F rudder, F canopy sill-to-stringer joint and the airbrake tests are described in more detail in the next chapters.

References

[1] Z. Kapidžić. A review of aeronautical fatigue investigations in Sweden during the period April 2017 to March 2019. Presented at the 36th Conference of the International Committee on Aeronautical Fatigue and Structural Integrity, Krakow, Poland, 2019.

[2] Z. Kapidžić. A review of aeronautical fatigue investigations in Sweden during the period April 2019 to March 2021. Presented at the 37th Conference of the International Committee on Aeronautical Fatigue and Structural Integrity, 2021.

2.2 Fatigue and damage tolerance testing of Gripen E/F rudder

J-E. Lindbäck[1], *Z. Kapidzic*[1], *R. Laakso*[2]

[1]Saab Aeronautics, Linköping, Sweden,
[2]VTT Technical Research Centre of Finland Ltd, Espoo, Finland

This chapter highlights the international cooperation research activities between Saab Aeronautics (Sweden) and VTT (Finland).

A structural test of Gripen 39E/F rudder was performed to verify the safe-life and damage tolerance of the rudder structure, see Figure 2.2-1. The test was performed in 2021-2022 in Finland in collaboration with VTT Technical Research Centre of Finland Ltd and its partners Eurofins Expert Services Ltd and Arecap Ltd, and the results are presented in the paper in [1]. Two different design load sequences, one representing the operational profile of 39E-version and the other for the 39F-version, with the latter being more severe, have been considered. Preliminary analyses have shown that a test using the more severe sequence 39F would likely not be able to verify the full service life. Therefore, a strategy was adopted to test the 39E sequence with upscaled loads during a part of the test campaign and thereby verify the 39E sequence, as well as part of the service life of 39F. The test was successfully run to a number of simulated flight hours [2, 3] where the most critical crack had grown from an artificial defect to a predicted critical length [4]. A subsequent static test showed that the structure had sufficient residual strength. The paper [1] presents an analytical procedure, based on fatigue and crack growth calculations, to determine the corresponding percentage of 39F service life that is considered to be verified by the performed test. This approach shows a cost-efficient way to utilize the test results as much as possible, without jeopardizing the primary goal of validating the configuration 39E of the aircraft.

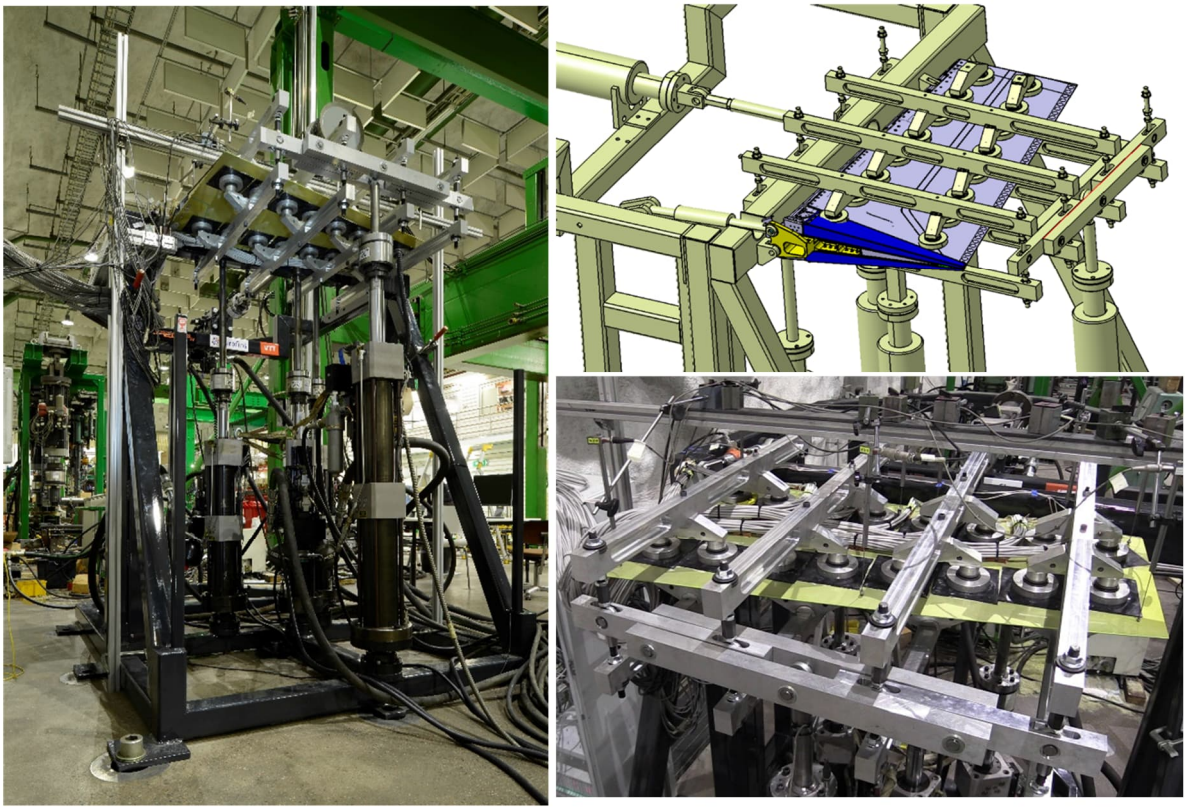

Figure 2.2-1. Rudder Fatigue and DT-test object and test rig.

References

[1] J. E. Lindbäck, Z. Kapidžić, A. Gustavsson, R. Laakso. Fatigue and damage tolerance testing of Gripen E/F rudder. Proceedings of the 31^{h} Symposium of the International Committee on Aeronautical Fatigue and Structural Integrity, Delft, Netherlands, 2023.

[2] J. Juntunen, R. Laakso. Description of tare procedure. Document № VTT-M-00873-21 (classified). VTT Technical Research Centre of Finland Ltd, (2021).

[3] R. Laakso, et al. Rudder Tests. Customer Report № VTT-CR-00133-20 (classified). VTT Technical Research Centre of Finland Ltd, (2022).

[4] T. Koskinen. Inspection report. [NDI on table after 5.75 design lives.] Customer Report № VTT-CR-00459-22 (classified). VTT Technical Research Centre of Finland Ltd, (2022).

2.3 Damage tolerance testing of Gripen F canopy sill-to-stringer joint

R. Rentmeester[1], *Z. Kapidzic*[1]

[1]Saab Aeronautics, Linköping, Sweden

Introduction

The canopy sill-to-stringer joint of Gripen F constitutes the upper part of the interface between the cabin and the aft part of the airframe, see Fig. 2.3-1. Hence, the joint as well as the included parts are critical from a safety point of view. The joint is located below the canopy, thus the effective height of the fuselage is limited. Also, the canard wings are situated just behind this joint. There are several contributions to the loads in the joint and the surrounding structure, such as global fuselage bending moment, cabin pressure and loads from the canard attachments.

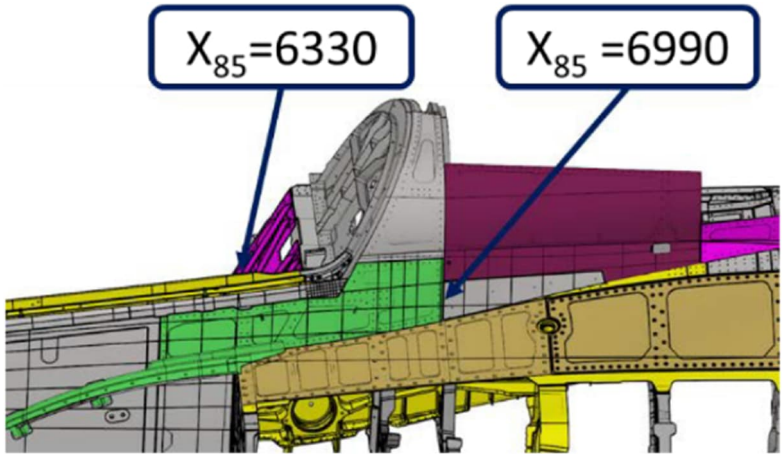

Figure 2.3-1. Outboard overview of the Gripen F airframe structure in the canopy sill-to-stringer joint area.

Since Gripen F is a twin seater aircraft, its canopy sill-to-stringer joint area is both larger, more complex and exposed to higher loads than the corresponding joint in the single seater version of the aircraft, cf. Fig. 2.1-7. It was therefore decided to divide the area into two parts and perform two tests in order to verify the full design life with respect to damage tolerance and fatigue. Figure 2.3-2 shows the overview of the joint area with the outer skins removed, where the to test areas, fwd-part Test 5.1.27.1 and aft-part Test 5.1.27.2 are indicated.

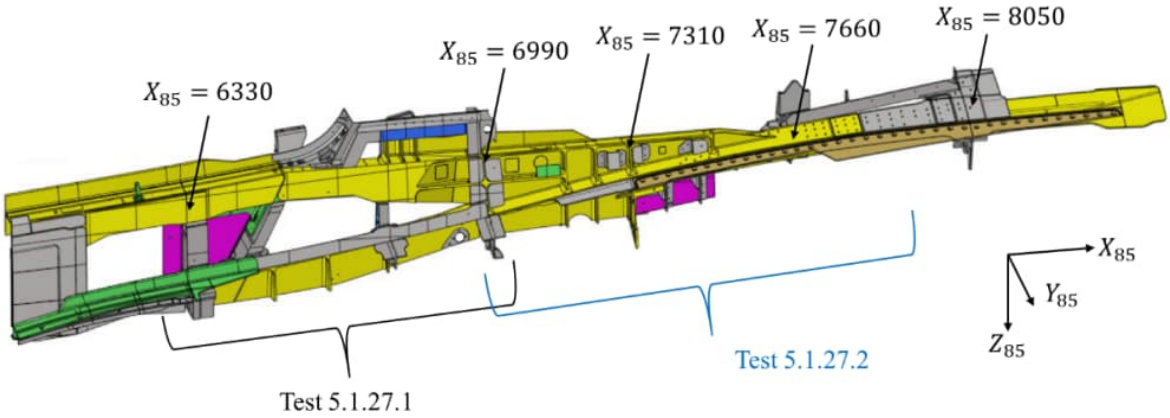

Figure 2.3-2. Outboard overview of the Gripen F airframe structure in the canopy sill-to-stringer joint area with the outer skin removed.

Loads

The loads and boundary conditions, as well as the structure itself, cannot be exactly represented in a test of integrated structure, in contrast to for example a control surface. The design of the test objects originate from the airframe design, with only minor changes to fit to the test rig. The major load paths were identified from the global finite element model of the airframe. The global FE model is coarse and local stresses are not suitable as target quantities. Instead, the overall load distribution, in terms of axial loads and bending moments were selected as target quantities to be simulated in the tests. The variation of the axial force in the primary test area was evaluated from the global finite element model for a representative load case that is expected to occur repeatedly during the use of the aircraft. Furthermore, the neutral line was calculated. The load application and the boundary conditions were designed in order to obtain the same neutral line and load variation along the primary test area in the test object.
It was difficult to test the complete structure in one test set-up, with only one or a pair of load actuators, and therefore two tests were defined and performed.

Test procedure

The forward test, see Fig. 2.3-3,was tested with focus on damage tolerance. In total 17 artifical defects were introduced by means of electro spark machining. Artificial defects in fastener holes and defects in geometrical features, such as in radii and on edges, were created. The test was run for 3.9 design lives in total, at a significantly elevated load for almost the whole second half of the test. Although several cracks grew during the test, no failure or unstable crack growth occurred in the finalizing static test to above the ultimate load level.

The aft test, see Fig. 2.3-4, was tested in fatigue. In this test two load actuators were used in order to refine the test quality further. It was tested for five design lives in total. The test started at nominal load with a gradually increasing load level. No artificial defects were introduced in this test object. Instead, the test object was significantly over-tested with respect to load level. The fifth design life was tested with a load sequence scaled with 1.5. No failure took place within the primary test area.

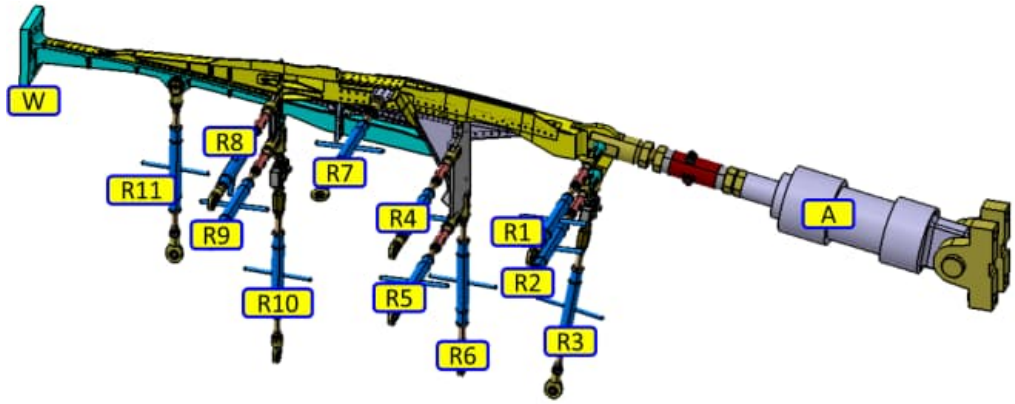

Figure 2.3-3. The forward test rig.

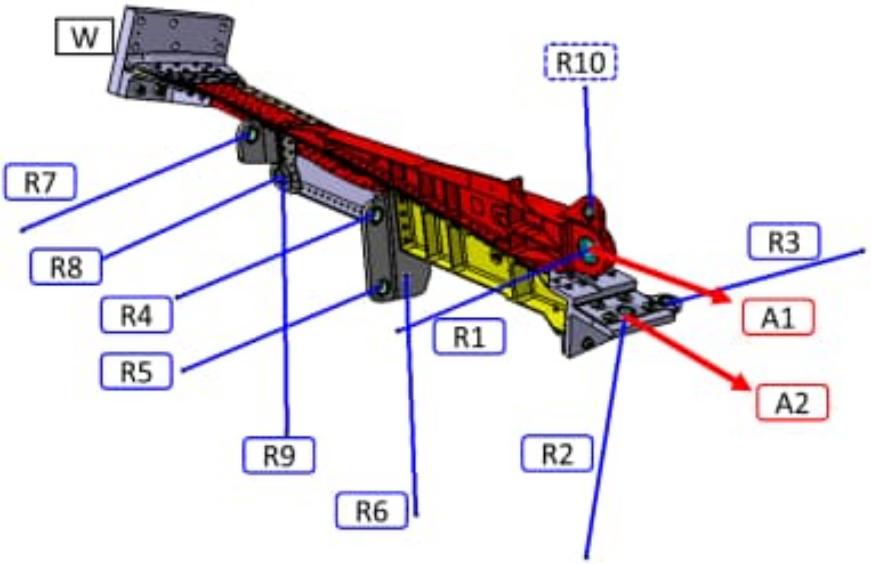

Figure 2.3-4. The aft test rig.

Conclusion

Both of the tests were successful from a verification point of view, meaning that the structures showed out to be robust from a fatigue respective a damage tolerance point of view. The load derivation strategy, i.e. evaluation of section forces instead of local stresses, was also considered successful.

It was concluded that both tests were rather complicated and required a great effort all the way from design to evaluation. One of the complexities are the boundary conditions. The lateral supports used in the two tests described herein were realized with rods with spherical bearings at both ends, see Figs 2.3-3 and 4. A greater portion of the airframe should perhaps be considered, which would provide more realistic boundary conditions in the primary test area.

2.4 Fatigue testing of Gripen E air brake

R. Rentmeester[1], *Z. Kapidzic*[1]

[1]Saab Aeronautics, Linköping, Sweden

Introduction

Airbrakes are used in order tune the speed of the aircraft. The airbrakes on the Gripen aircraft are integrated on both sides of the aft fuselage, see Fig. 2.4-1.

Figure 2.4-1. Gripen E, air brake marked with red circle.

They are activated through a rotation about a vertical hinge line by an actuator on each respective side. The Gripen airbrake is designed to be used in tactic flight maneuvers as well as to slow down before landing, and it is not always fully deployed. This results in a variety of air loads acting on the airbrake. Also it leads to a varying force from the deployment actuator, regarding both magnitude and direction relative to the airbrake. Due to its position with respect to the airframe, the design space for the airbrake is limited. It is designed as a metallic structure made up of a single skin that is reinforced by two frames and the attachments to the hinge line. This design allows for relatively large deformations of the structure, which are demanding when it comes to testing.

Test procedure

It is not feasible to rotate the airbrake around the hinge line during the test, as is the case in the real usage. The airbrake was therefore installed in a test rig with the same boundary conditions as in the airframe installation, see Figs. 2.4-2 and 3. The air loads were applied by two independent actuators, Act_1 and Act_2. They were positioned on a predefined distance from the hinge line. The distance was selected to represent the pressure center of the air loads for the majority of the conditions. The loads were transferred from the two actuators to the airbrake via two whiffle trees, shown in orange and blue in Figs. 2.4-2 and 3. Effort was made in order to stabilize the whiffle trees, since they were primarily loaded in compression and the airbrake was deformed to a significant degree also under nominal load.

The Act_1 and Act_2 loads were derived so that the moment about the hinge line and the moment about an axis perpendicular to the hinge line, along to airbrake, were equal to the calculated moments in the global load sequence. Since the moment about the hinge line was used as a target quantity, it was possible also to apply the correct load on the lug on the airbrake where the deployment actuator is attached. However, this required a specially designed interface to the test rig, see Fig. 2.4-3. The rotation around the hinge line was constrained by a

load cell, a Jack. Along with the hinge line boundary conditions, the Jack constitutes a complete set of boundary conditions, meaning that all rigid body motions are constrained. The Jack was equipped with a load cell, in order to ensure that the correct loads were applied and that the whiffle trees worked as expected.
A third actuator, Act_3, was installed in the same lug on the airbrake as the Jack. The Act_3 loads were derived so that both the magnitude and direction of the resulting load on the airbrake lug were correctly achieved. This arrangement worked well and was stable. However, note that there was no compressive loads acting from Act_3.

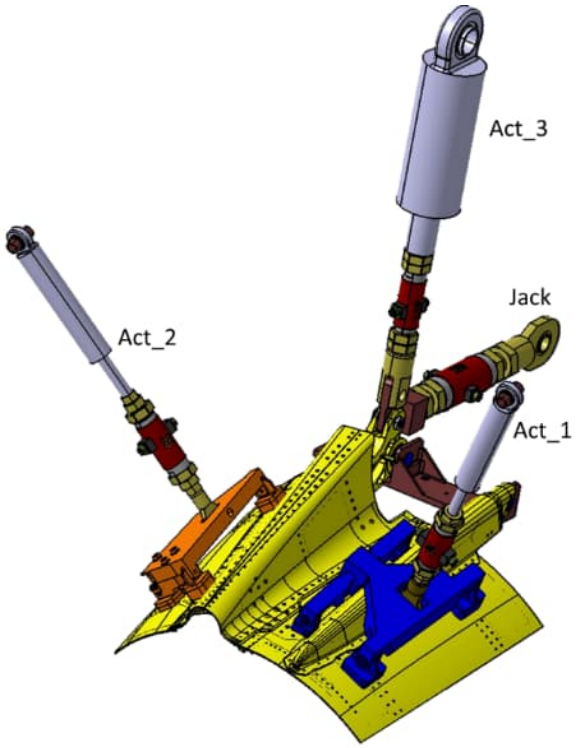

Figure 2.4-2. Air brake test object and the load actuators, top view.

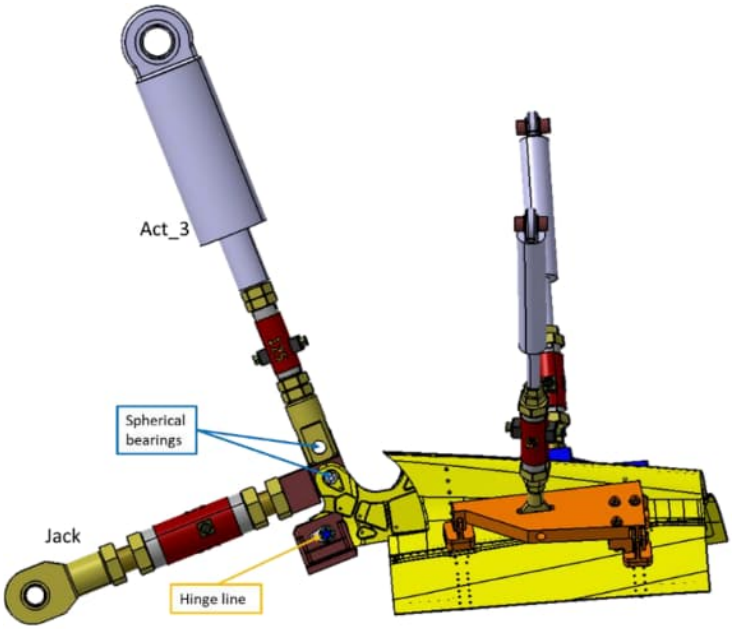

Figure 2.4-3. Air brake test object and the load actuators, side view.

One of the primary goals of the test was to investigate the fatigue properties in the bolted joints in the airbrake. The bolted joints are subjected to high loads due to twisting of the airbrake. The test was successful regarding the bolted joints.

3 TESTING AND MODELLING OF BOLTED JOINTS

3.1 Fatigue testing of aluminum bolted joints with over-sized holes

Z. Kapidzic[1]

[1]Saab Aeronautics, Linköping, Sweden

Introduction

In contrast to co-drilled fastener holes, over-sized holes are manufactured separately in each plate and will generally obtain greater clearance and possibly axis offset from the intended fastener positions. In a multi-fastener joint, the greater clearance and offsets may result in unexpected fastener load distribution where some fasteners may transfer higher loads than anticipated. Locally, the loads might transfer through the fastening points so that the local stresses in the plates and the fastener are increased. Both of these effects can potentially decrease the fatigue life and need therefore to be understood and accounted for in sizing.

The primary aim of this study was to investigate the effects of the oversized holes on fatigue. An experimental study was conducted on joint specimens where the mentioned effects are purposely introduced in order to study their effects on fatigue life. A fatigue life prediction model for joints with tolerance fitting, shown in chapter 2.8 in [1] and in [2], was used for evaluation and comparison to current testing results.

Test specimens

All specimens were made of AA7050-T7451 thick plate material as single shear, 6x2 butt joints with fasteners with protruding bolt heads, see Fig. 3.1-1 for specimen drawing. Five different specimen configurations were tested, including specimens with Ti-screws with hexagon head or Hi-Lites and with or without plate surface treatment TSA (Tartaric Sulphuric Acid) and sealant between the plates. Table 3.1.1 shows the test matrix with the five specimen configurations (types), number of tested specimens, fastener type, and dimensions. The table also shows the over-sized hole diameter for each specimen configuration. All holes in all specimens were manufactured by machining and afterwards co-reamed to over-size diameter. All fasteners were pre-tightened to approximately 6 Nm torque.

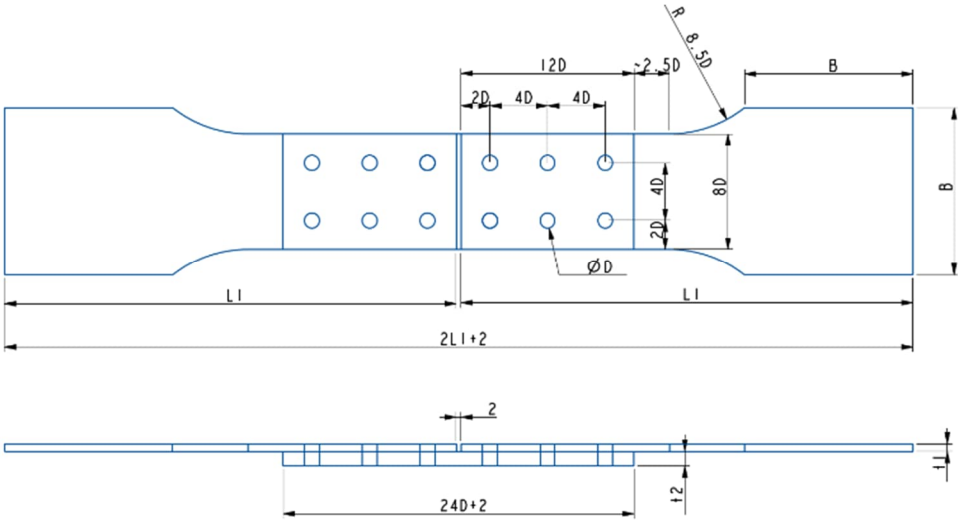

Figure 3.1-1. Specimen drawing, with bolts removed for visibility.

Table 3.1-1. Test matrix.

Spec type	Nbr of spec	Fastener type	Surface treatment	t1 [mm]	t2 [mm]	D [mm] (actual hole diameter in paranthesis)
S6	6	Ti-screw		3.00	6.00	6 (6.2)
H6	6	Hi-Lite		3.00	6.00	6 (6.14-6.34)
H5	6	Hi-Lite		3.00	6.00	5 (4.8+0,14/ +0,34)
S6T	6	Ti-screw	TSA	3.00	6.00	6 (6.2)
S6TS	6	Ti-screw	TSA/Sealant	3.00	6.00	6 (6.2)

Test procedure

All tests were performed in a uniaxial tensile/compressive machine. Before the specimens were mounted in the machine, a lateral support device was installed on each specimen, see Fig. 3.1-2, to reduce the secondary bending. The support comprised two steel support profiles that were in contact with the upper and the lower surfaces of the specimen. The support profiles were connected by four M10 bolts and were mounted using two nuts on each bolt. The nuts were tightened and adjusted so that the specimen was in contact but could slide between the supports by hand force. Also, a lubricant spray was applied to reduce the friction between the specimen and the support. The specimens were gripped at the ends and the load was applied in force control.

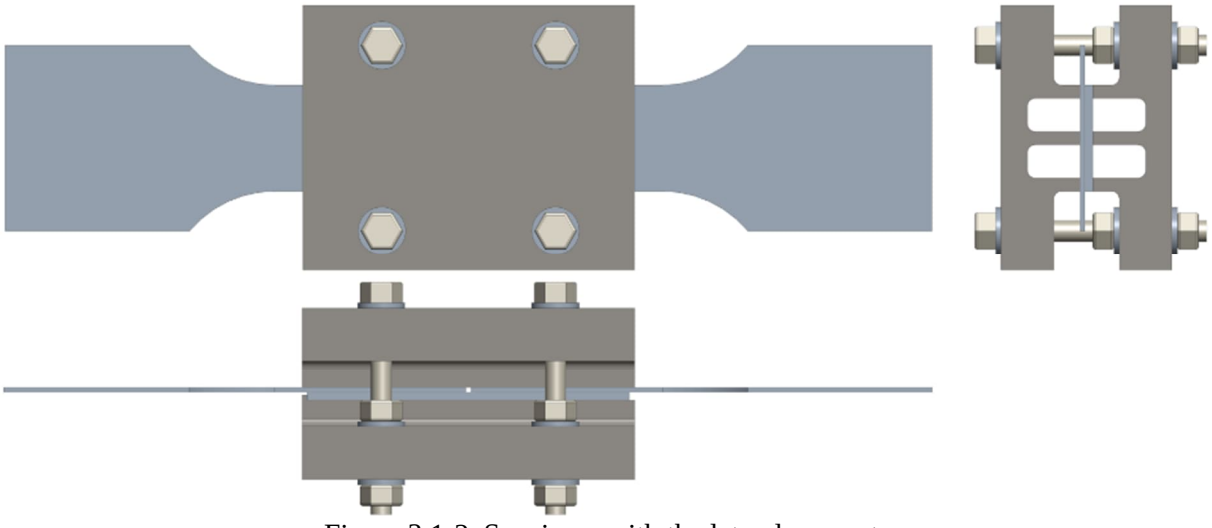

Figure 3.1-2. Specimen with the lateral support.

All specimens were tested at room temperature using a tensile dominant variable amplitude load sequence, representing a fighter wing bending moment and containing around 60 cycles/flight hour. Figure 3.1-3 shows the level exceedance plot for 1000 flight hours of test sequence. The specimens were tested to failure a several different maximum sequence stress levels at cycling frequencies in the range of 10-13 Hz.

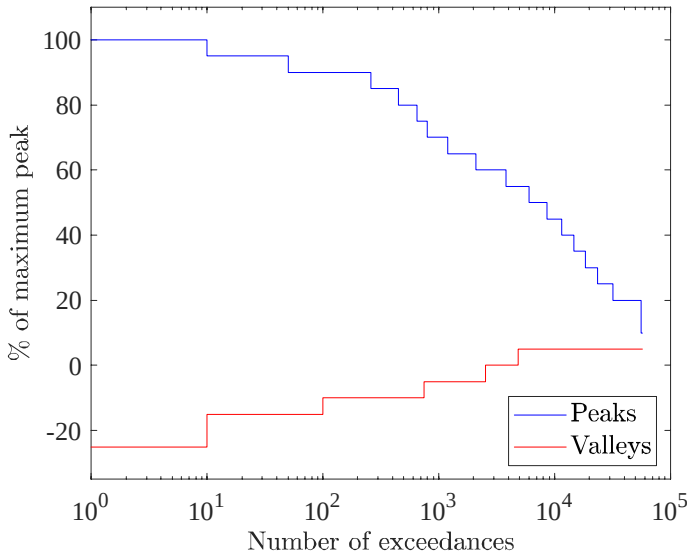

Figure 3.1-3. Level exceedance plot for 1000 flight hours of test sequence.

Results

All specimens failed by fatigue cracking of one of the skin plates, in the vicinity of the outermost bolt row. The fatigue cracks typically initiated in the faying plane surface of the skin plate, at a small distance from the bolt hole and then grew throught the plate, as shown in Fig. 3.1-4.

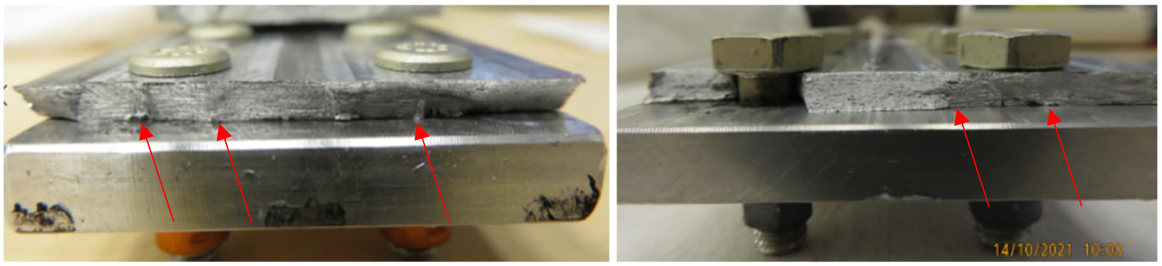
Figure 3.1-4. Typical fatigue failure of the skin plate. Red arrows indicate the crack initiation points.

Similar behaviour was observed in [1] and [2] in properly clamped joints, while losely clamped joints developed fatigue cracks at the hole edge and had typically shorter fatigue life. A conclusion was drawn that a sustained clamping force promotes load transfer by friction between the plates, which lowers the load transfer thorugh the fastener-hole interface and increases the fatigue life. From the characteristics of the fatigue cracking, it can be inferred that the currently tested joints were also properly clamped and that their fatigue perfromance should be similar to the performance of joints with tolerance fitting.

To confirm this, we compared the predicted fatigue life, using the model form [1] and [2] for joints with tolerance fitting, to the current test results, see Fig. 3.1-5. The figure shows the predicted mean life and the lower and upper bounds of 3 standard deviations. All test results are within the 3σ bounds and most of the test results correlate well with the mean curve. There is no apparent difference between the different joint configurations with Ti-screws and the Hi-Lite joints performed slightly better.

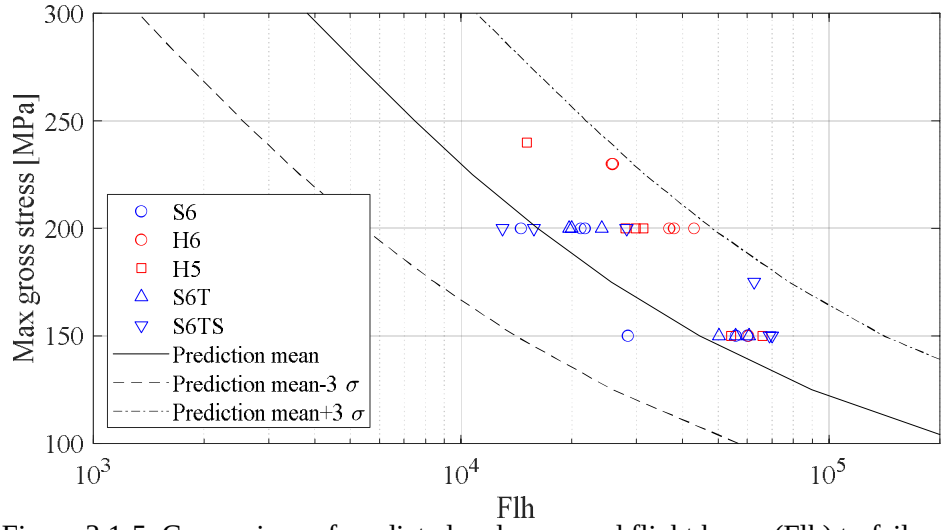

Figure 3.1-5. Comparison of predicted and measured flight hours (Flh) to failure.

Conclusion

An experimental study of aluminum joints with over-sized holes was performed. The experimentally obtained fatigue life and the predicted life, using the model from [1] and [2] for joints with tolerance fitting, correlated well. It can be concluded that the over-size holes seemingly had no detrimental effect on the joint fatigue life.

References

[1] Z. Kapidžić. Development of data and method for fatigue sizing of bolted joints in AA7050-T7451 and AA2050-T84. In: A Review of aeronautical fatigue investigations in Sweden during the period April 2017 to March 2019, 36th ICAF Conference, Krakow, Poland, 2019.

[2] Z. Kapidžić. Comparison of fatigue life and flexibility between aluminum-composite and aluminum–aluminum bolted joints, International Journal of Fatigue, 157, 106695, 2022.

3.2 Fatigue of Aluminum-CFRP bolted joints

Z. Kapidzic[1]

[1]Saab Aeronautics, Linköping, Sweden

Introduction

Reference [1] presents a study of fatigue behavior of shear-loaded bolted aluminum-aluminum (A-A) joints and proposes a semi-empirical model for prediction of fatigue life of A-plates. The fatigue process is described as complex and dependent on a combination of several factors: stress concentrations at bolt locations, contact and fretting corrosion, load eccentricities, bolt pretension and load transfer by friction. In a A-CFRP joint, the fatigue behavior of the Al-plate may differ compared to an A-A joint due to: different stiffness of A and CFRP, additional fatigue mechanisms introduced by the CFRP and different frictional conditions at the plate interfaces. Also, there is a risk of pretension relaxation due to viscoelastic effects in CFRP. The study presented in [2] investigated if the fatigue performance of the A-plate is impaired in the presence of neighboring CFRP-plates and main findings are presented in this chapter.

In [2], A-A and A-CFRP joints were fatigue tested in variable amplitude loading and the relative displacement between the middle plates was measured continuously. Solid finite element (FE) models of the joints were used for simulation of the displacements and to study the effects of the friction on the joint behavior.

Test specimens and testing procedure

The test specimens were double-shear butt-joints with four rows and two columns of protruding head titanium bolts, see Fig. 3.2-1. In all specimens, the middle plate was made of aluminum and was the critical plate were the fatigue failure took place. All fastener holes were co-drilled to near full size and co-reamed before assembly, when a pre-torque of 6 Nm was applied to all bolts. The specimens were tested one year after the assembly, to allow time for pretension relaxation to take place. An extensometer was attached with one leg on each of the middle plates in the middle of the specimen and was used to measure the relative displacement, δ, between the middle plates. The same tensile-dominant load sequence as in the previous chapter, see Fig. 3.1-3, was applied on all specimens. Recurringly after every 1000 flight hours of cycling, the sequence loading was interrupted to apply a 0-tension-compression-tension-0 load cycle, during which the relative displacement was measured with high sampling rate. The relative displacement was also measured continuously during the sequence loading, at maximum and minimum load states.

Figure 3.2-1. A-A (upper) and A-CFRP (lower) specimens, fatigue cracks are marked by arrows, figure from [2].

Results

Interestingly, the continuously measured relative displacement at maximum and minimum load states decreased during the sequence loading in both specimen types. Figure 3.2-2 shows the flexibility $C_\Delta = \Delta\delta/\Delta F$ (relative displacement range normalized by the applied force range) as function of the tested flight hours. The decreasing flexibility was explained by increasing friction during the fatigue loading.

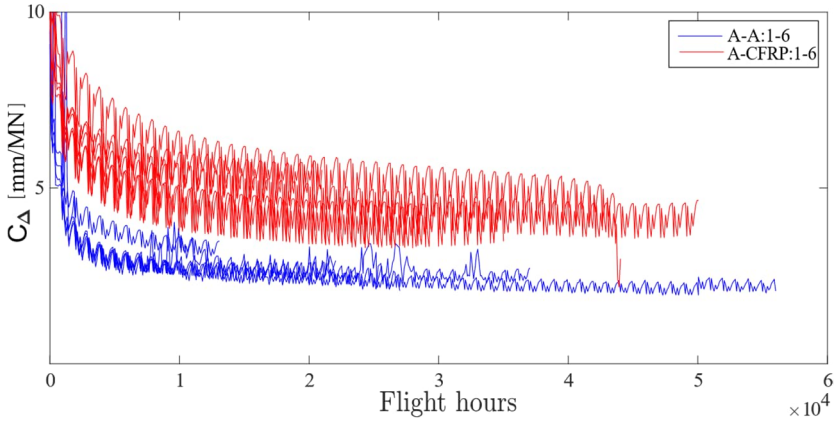

Figure 3.2-2. Flexibility during continuous measurements, figure from [2].

Similar trend was observed during the recurring measurements every 1000 flight hours. Figure 3.2-3 shows that the force-relative displacement during the first measurement at 0 flight hours (denoted with i =1 in the figure) differs from the following measurements. During i = 1, three different phases can be identified in the hysteresis loop: sticking, slipping and load transfer. For i > 1, the relative displacement range is significantly smaller than for i = 1, for both specimen types and the loops are open. Also a larger relative displacement range is observed for A-CFRP specimens than for A-A specimens.

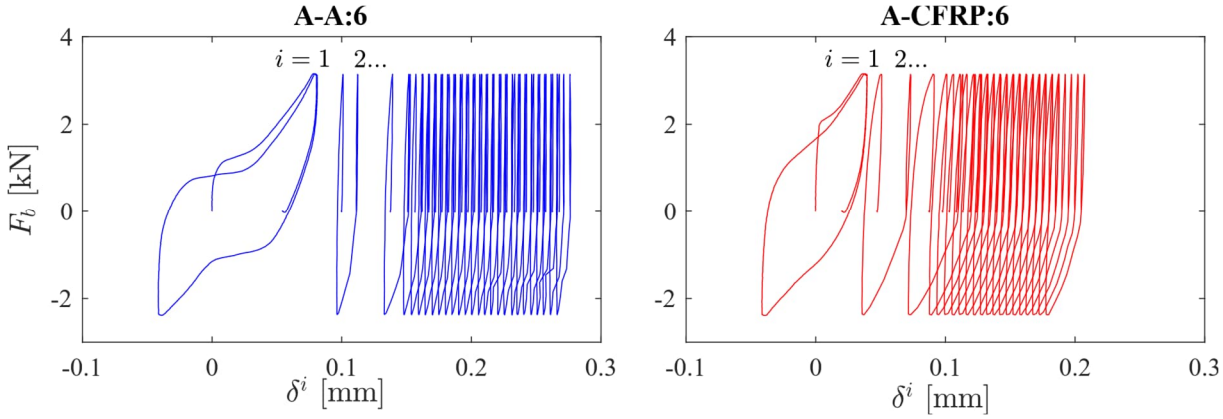

Figure 3.2-3. Force-relative displacement during recurring measurements every 1000 flight hours, figure from [2].

FE-simulations were performed for a range of different coefficients of friction, μ, at the plate interfaces. For μ = 0.2, a similar hysteresis loop as measured in the tests was obtained, see Fig. 3.2-4. The difference between the FE-results and the measurements was attributed to different amount of clearance in the model and in the test specimens. Apart from that, the three phases in the simulated loop are clearly identified. Changing the coefficients of friction resulted in different loops but they were all closed. However, when μ was allowed to be dependent on the load direction an open loop is obtained. Figure 3.2-4 shows the comparison for μ = 0.65 in

tensile loading and μ = 0.45 in compression for A-A specimen and μ = 0. 5 in tensile loading and μ = 0.35 in compression for A-CFRP specimen.

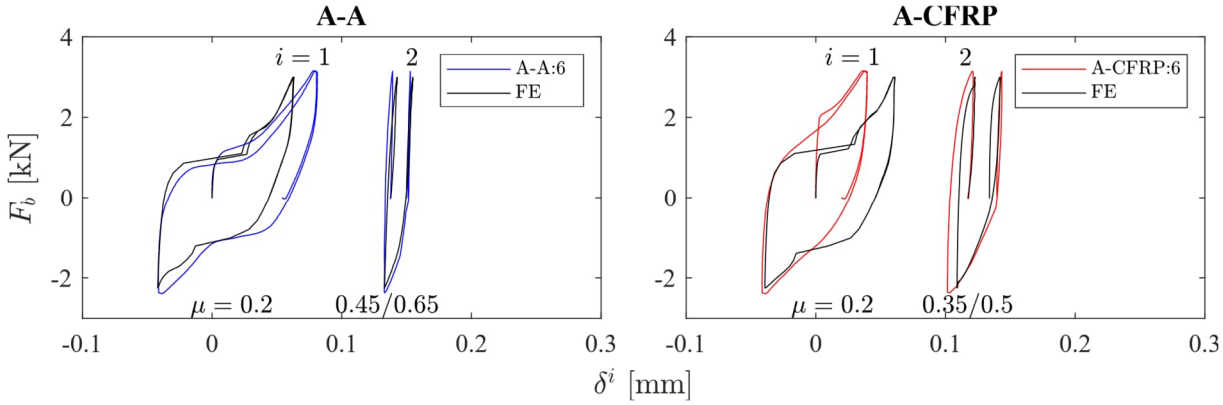

Figure 3.2-4. Force-relative displacement during recurring measurements at 0 and after 1000 flight hours compared to FE-results, figure from [2].

The fatigue life for both specimen types correlated well with the predictions by model in [1]. Thus there was no apparent effect of the neighboring CFRP-plate on the fatigue life of the A-plate. Conclusively, the study showed that load transfer by friction is load direction dependent and that it changes during the fatigue cycling.

The work is supported by the Sweden's Innovation Agency by grant agreement No. 2020-00187.

References

[1] Z. Kapidžić. Development of data and method for fatigue sizing of bolted joints in AA7050-T7451 and AA2050-T84. In: A Review of aeronautical fatigue investigations in Sweden during the period April 2017 to March 2019, 36th ICAF Conference, Krakow, Poland, 2019.

[2] Z. Kapidžić. Comparison of fatigue life and flexibility between aluminum-composite and aluminum–aluminum bolted joints, International Journal of Fatigue, 157, 106695, 2022.

3.3 Bolt fatigue in CFRP-CFRP joints

Z. Kapidzic[1]

[1]Saab Aeronautics, Linköping, Sweden

Introduction

Carbon fiber reinforced polymer (CFRP) plates are commonly joined using titanium bolts. As sizing against static failure of CFRP is normally done considering the ultimate load, fatigue is rarely a problem for joined CFRP plates at operational loads. However, titanium bolts are prone to fatigue in CFRP joints with large thickness-to-diameter ratios, where bolt bending stresses may be significant. Moreover, application of liquid shim between mating surfaces of CFRP plates further increases the clamping length of the bolts and potentially lowers the load transfer by friction between the plates. Both of these effects increase the bolt bending stress amplitude in fatigue loading.

The study in [1] presents an analytical model for calculation of bending stress in protruding- and countersunk-head bolts in single- and double-shear joints, with or without liquid shims. Solid FE-models were used to validate the analytical model. Further, a semi-empirical fatigue life equation, based on the calculated bending stress amplitude, was fitted to results from constant amplitude fatigue tests performed on single-shear CFRP specimens with titanium bolts. The tests included specimen variants with and without liquid shim, with standard or finger-tight pretension, and with and without a teflon tape between the plates. Finally, predictions of variable amplitude fatigue life are performed and compared to experimental results from the literature. This chapter summarizes the procedure and the main findings from the study in [1].

Analytical model for calculation of bolt bending stress

The bolt bending problem is shown in Fig. 3.3-1, where $v(x)$ is the displacement of the bolt centerline measured from the undeformed, translated bolt configuration shown in red. The contact force per unit length, $q(x)$, is exerted by the bolt on the hole edges. Considering the force and the moment equilibrium of the bolt shank, assuming that the bolt shank is a Timoshenko beam and assuming that the contact force is proportional to the bolt displacement, the following differential equation is obtained

$$A_4 \frac{d^4 v}{dx^4} - A_2 \frac{d^2 v}{dx^2} + A_0 v = 0$$

where the coefficients depend on the elastic and geometric properties of the bolt, the plates and the shim. The above equation is solved for the three segments 1, 2 and 3, for an applied bolt force P_b. From the solution of the displacement $v(x)$, the bending moment $M(x)$, the shear force $T(x)$, the contact force $q(x)$ and the rotation of the bolt $\psi(x)$ are calculated, as shown in [1]. The solution assumes continuity of $M(x)$, $T(x)$ and $dv/dx(x)$ at the segment interfaces and elastic boundary conditions at the outer surfaces $M(x = 0) = -\lambda_1 \psi(x = 0)$ and $M(x = t_1+t_2+t_3) = \lambda_3 \psi(x = t_1+t_2+t_3)$. The rotational restraint factors λ_1 and λ_3 are functions of the total clamping thickness and are computed using solid FE-models of the problem. For a countersunk bolt, with the countersunk depth of x_{cs}, the problem is solved by only considering the thickness of the plate with the cylindrical part of the hole edge. Figure 3.3-2 shows a comparison of the normalized bending moment over the thickness between the analytical and the FE-model.

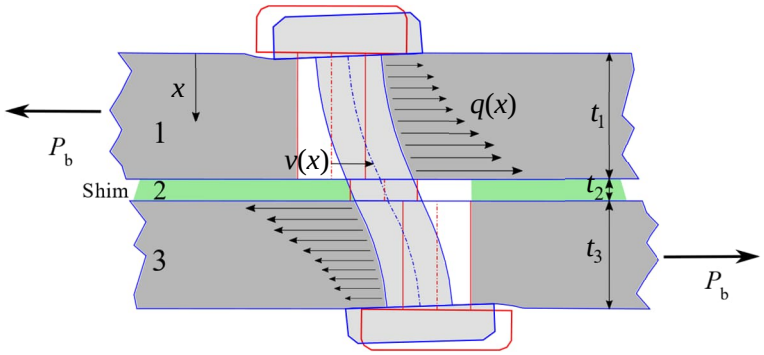

Figure 3.3-1. Bolt bending in a single-shear joint with a shim layer, figure from [1].

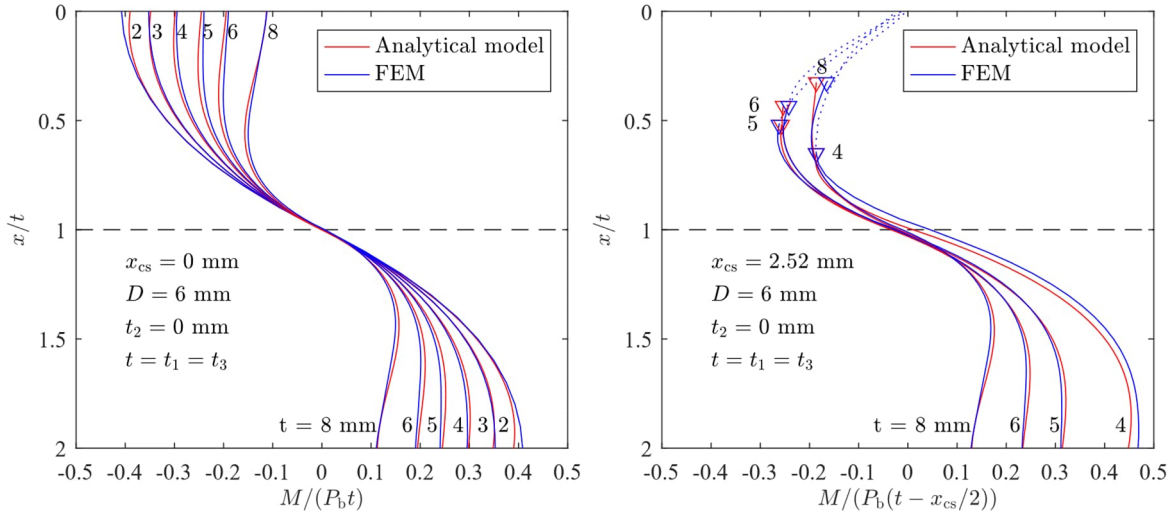

Figure 3.3-2. Comparison of normalized bending moment between the analytical and the FE-model, for protruding bolt head (left) and countersunk bolt head (right), figure from [1].

Test specimens, testing procedure and test results

The test specimens two-row, two-column single-shear butt joints with two CFRP skin plates and one CFRP butt plate. Seven specimen configurations were tested including, different skin thickness t_1, liquid shim thickness t_2, bolt pretension torque, and with or without and teflon tape. The fastener holes were co-drilled to near full size and thereafter co-reamed to H10 tolerance. The bolts were countersunk-head, titanium Ti–6Al-4V bolts with a nominal diameter D = 6 mm and were installed and tightened with a torque wrench to 6.3 Nm (normal torque) or 2 Nm (finger-tight). Most of the specimens were tested with a lateral support device, such as that shown in Fig. 3.1-2, to reduce the secondary bending. All specimens were fatigue tested to failure in a tensile/compressive machine at constant amplitude, with an applied load ratio of −0.25. During the testing, the grip displacements were recorded at every load reversal.

In normally torqued specimens (6.3 Nm), without liquid shim or teflon tape, the grip displacement range normalized by the applied force range (flexibility) decreased after a few hundred cycles and remained thereafter almost constant until failure. This was attributed to increased friction and load transfer by friction in the plate interfaces. A constant or even increasing flexibility was measured in all other specimen variants, where lack of friction increase was expected. They also had relatively shorter fatigue lives. All specimens failed by bolt fatigue, where fatigue cracks initiated under the countersunk bolt heads, as shown in Fig. 3.3-3, and no fatigue damage was detected in the CFRP plates.

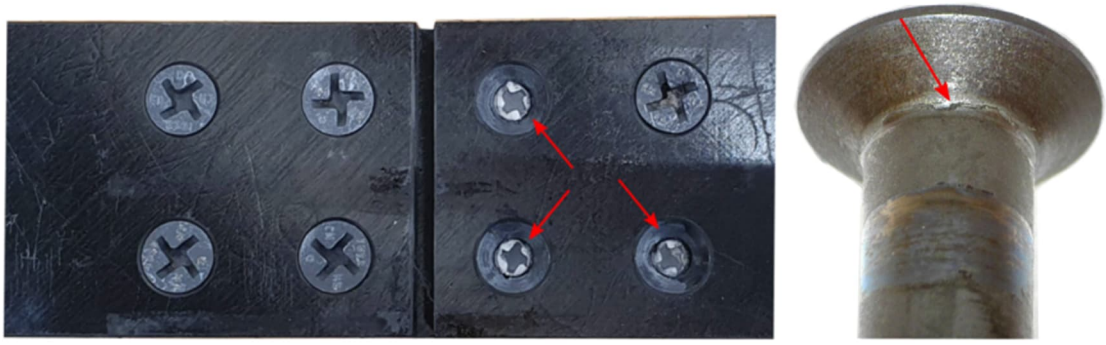

Figure 3.3-3. Bolt fatigue, figure from [1].

Fitting of fatigue life equation and comparison to variable amplitude tests

For every specimen type, the stress variation under the bolt head was calculated using the analytical model and taking into account the load transfer by friction, pretension and the stress concentration. The calculated stress amplitude, stress ratio, stress concentration factor and tested number of cycles to failure were used to fit an S-N type equation. Besides the tests performed in [1], tests on joints with protruding-head bolts from literature were included in the fitting. Finally, the resulting S-N equation together with the linear cumulative damage rule were used to predict variable amplitude fatigue life of double-shear joints with protruding-head bolts. The results corresponded well with the test results from the literature and the comparison can be found in [1].

The work is supported by the Sweden's Innovation Agency by grant agreement No. 2020-00187 and was performed as a collaboration between Saab AB in Sweden and CIAC and University of Los Andes in Colombia.

References

[1] Z. Kapidžić, D. L. Ávila Granados, J. A. Moreno Arias, M. J. Quiroga Aguilera, J. P. Casas Rodríguez, J. C. García Callejas. Bolt fatigue in CFRP joints, International Journal of Fatigue, 164, 107138, 2022.

3.4 Experiments and modelling of CFRP-aluminum bolted joints

H. Wemming[1,2]

[1]Saab Aeronautics, Linköping, Sweden
[2]Solid Mechanics, Linköping University, Linköping, Sweden,

Introduction

This chapter summarizes the research presented in the licentiate thesis in [1]. The aim of the research is to improve the understanding of shear-loaded, composite–aluminium, bolted joints in terms of structural compliance, deformation, load distribution, strength and failure, by performing experiments and developing models to simulate the observed joint behavior. Experiments are performed and the optical digital image correlation (DIC) technique is used to measure the deformation of the test specimen surface during quasistatic load to failure. The DIC method enables more detailed deformation measurements compared to conventional methods such as extensometer measurement. Data processing algorithms for noise reduction of DIC measurement data are developed and the results are used in a novel way to detect the onset of bearing damage within the material by observing the specimen surface. The experimental DIC data is also used for adapting models, where the goal is to create a structural element that represents a fastener. Structural elements are computationally efficient and suitable for implementation in large scale models of airframe structures in an industrial context. A model is proposed and the selection of parameters are investigated and fitted to experimental data.

Bearing damage detection using DIC

In reference [2] quasistatic failure of single-shear, two-bolt lap composite-aluminium bolted joints are investigated experimentally using the stereo DIC technique. The displacements are measured and processed to reduce the noise by taking advantage of specimen symmetry. The localized curvature of the specimen surface near the bolt holes, that arises as a result of bearing damage, is measured and quantified as the Gauss curvature parameter K_G. Thus, a sudden change of the Gauss curvature is used as an indicator of bearing damage onset. Figure 3.4-1 shows an example of measured Gauss curvature parameter, its variation as a function of the bearing stress and the point of bearing damage onset.

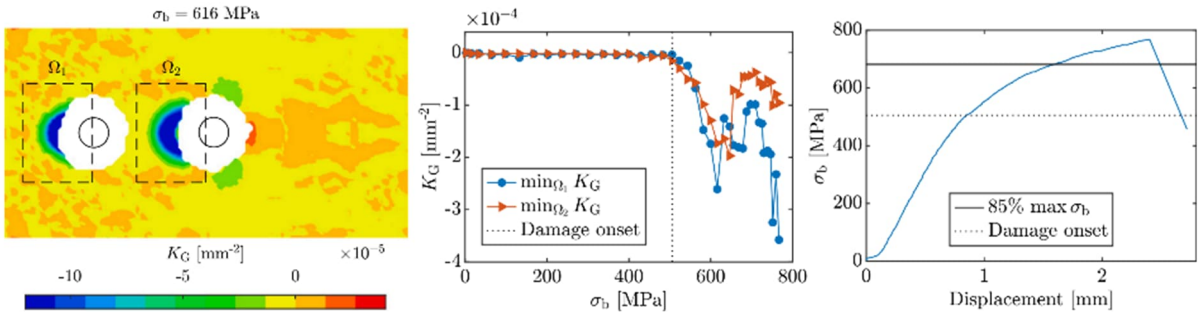

Figure 3.4-1. Gauss parameter K_G measured by DIC (left), K_G as function of the bearing stress σ_b (middle) and bearing stress-displacement curve (right), figure from [2].

Modelling of fastener installation behavior based on DIC measurements

The study in [3] explores the possibility of using an Iwan-type model to represent behavior of the fastener installations in CFRP–aluminium bolted joints subjected to uniaxial quasistatic tensile load up to failure. The DIC technique is used to measure the joint displacement. A

suitable distribution function in the Iwan model is found and model parameters are identified so that the displacements fit the experimental DIC results. The resulting structural element representing bolt installations is applied to two-bolt lap joints and a comparison between the experimental and predicted displacements of the bolted joints is presented. It is also demonstrated that the structural element can be implemented in a commercial FE software. Figure 3.4-2 shows a model, where the plates are represented by beam elements and the fastener installations by Iwan elements, and a comparison of the force-displacement curves from the said model, test and the implementation in Abaqus using shell elements. It is concluded that an Iwan model can be used to represent fastener installations in CFRP–aluminium bolted joints and predict the forces and displacements of the joint.

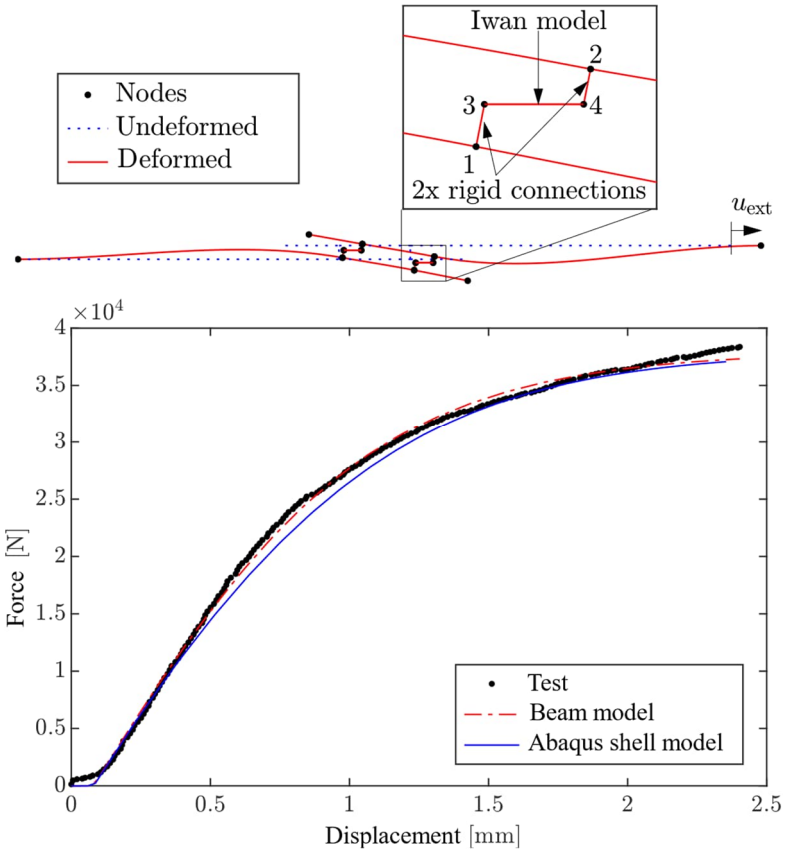

Figure 3.4-2. Beam model om a single-shear joint with two bolts (upper) and comparison of force-displacement (lower), figure from [3].

The work is supported by the Sweden's Innovation Agency as grant agreement No. 2017-04877.

References

[1] H. Wemming. Experiments and modelling of composite–aluminium bolted joints. Linköping University Electronic Press, 2022. (Linköping Studies in Science and Technology. Licentiate Thesis.)

[2] H. Wemming, S. B. Lindström, L. Johansson, Z. Kapidžić. Identification of bearing failure in composite–aluminium bolted joints using digital image correlation, Composite Structures, Volume 300, 116072, 2022.

[3] H. Wemming, S. B. Lindström, L. Johansson, Z. Kapidžić. Modelling and experimental parameter identification for fasteners in composite–aluminium bolted structures, submitted to Composite Structures, 2023.

3.5 Testing of repairment method EPOCAST for incorrectly drilled bolt holes in CFRP joints

Z. Kapidzic[1]

[1]Saab Aeronautics, Linköping, Sweden

Carbon fiber reinforced polymer (CFRP) plates are commonly joined using bolted connections. In large airframe panels the connections can have a large number of bolts which are installed after co-drilling the plates. During the drilling operation, there is a risk that the bolt holes can be incorrectly drilled. For example, a hole can be mislocated, drilled with an angularity outside of tolerance or too deeply countersunk. In such cases a repairment might be an option. However, the effect of the repairment on the strength of the joint need to be accounted for.

In the proposed study, a two-step repairment technique using Epocast potting is to be investigated. Epocast 1635 consists of a two-component epoxy resin that is mixed with aluminum powder. It can be applied using a mixing nozzle to ensure a good mixture of components. The repair is performed in two steps by first repairing the incorrectly drilled hole and then drilling a correct hole, partially through the repair. Figure 3.5-1 shows an example of the repairing procedure and a repaired countersunk hole.

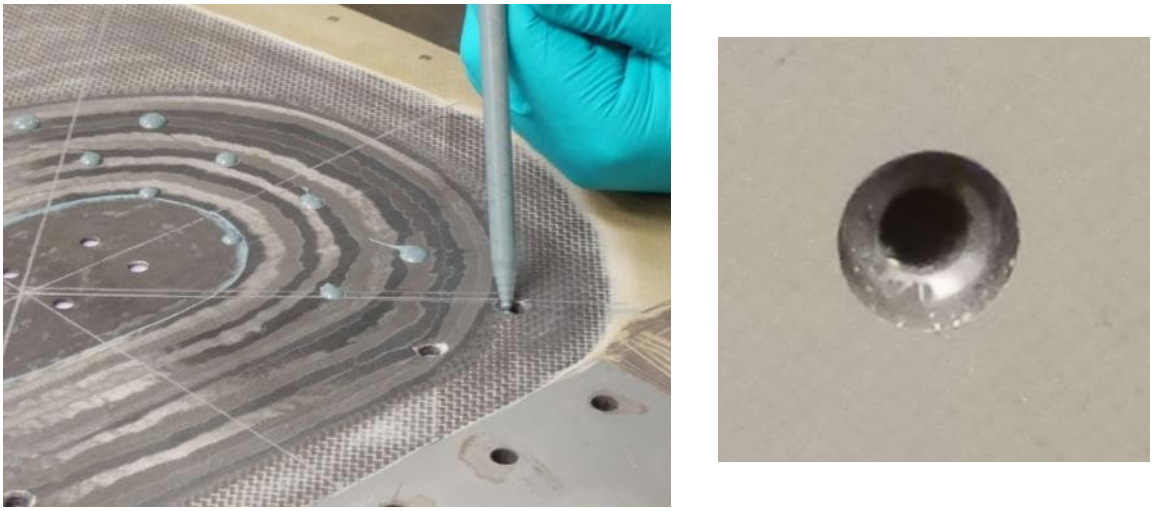

Figure 3.5-1. Repairing of incorrectly drilled holes using Epocast potting.

The proposed study aims at establishing knock-down factors for bearing strength, net-section strength and fatigue strength of repaired holes. Three different types of incorrect drilling will be considered, as shown in Fig. 3.5-2. The study will be performed on standard specimens and will include variations of laminate layup, thickness, hole diameters, static, constant amplitude and spectrum loading. The study will be performed during 2023-2024 as a collaboration between Saab AB in Sweden and CIAC and University of Los Andes in Colombia.

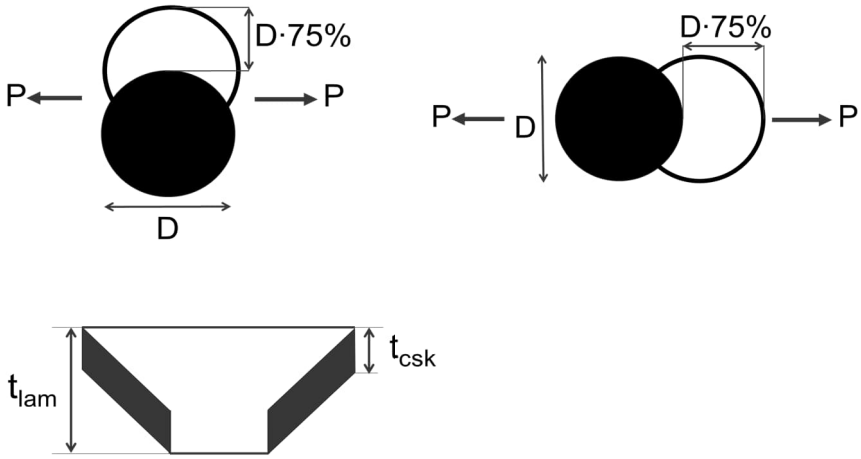

Figure 3.5-2. Types of incorrectly drilled holes.

4 FATIGUE AND CRACK GROWTH MODELLING

4.1 Method for calculation of stress intensity factors for cracks in multi-fastener joints

Z. Kapidzic[1], *E. Fernandez Rodriguez*[1]

[1]Saab Aeronautics, Linköping, Sweden

Introduction

The phenomenon of aging structures has brought attention to the problem of widespread fatigue damage (WFD) and multiple-site damage (MSD). The damage scenario involves numerous small MSD cracks and a lead crack which can interact and significantly degrade the damage tolerance and reduce the load for unstable crack propagation. Of particular interest is the problem of bolted or riveted multi-fastener lap joints in aircraft fuselages. Typical fuselage geometry includes thin aluminum sheet panels joined by multiple rows of fasteners. The MSD scenario involves cracks emanating from the fastener holes and simultaneously growing through a fastener row due to the load transferred by the joint. The problem is usually analyzed using fracture mechanics and the concept of stress intensity factor (SIF). Fracture mechanics software, such as AFGROW, offer a possibility to analyze crack growth scenarios with multiple fastener holes. However, the available scenarios are restricted to regular fastener hole patterns, limited number of fastener holes with the same diameter and normal loading. More complicated scenarios can be solved using commercial finite element (FE) software but that requires a considerable pre- and post-processing effort. The work in [1] presents an automated FE-based approach to solve the plane MSD problem with multiple fastener holes. This chapter presents a summary of the work in [1].

FE-model

An FE-program for plane stress problems is written in MATLAB. The program contains a mesh function that can create a structured element mesh for a rectangle with or without a hole, as shown in left Fig. 4.1-1. A mesh for a geometry with multiple holes is built up by merging of multiple rectangles, see right Fig. 4.1-1. The meshing process is functionalized and requires user input in terms of number, locations and diameters of the holes, hole spacing, plate width and height etc.

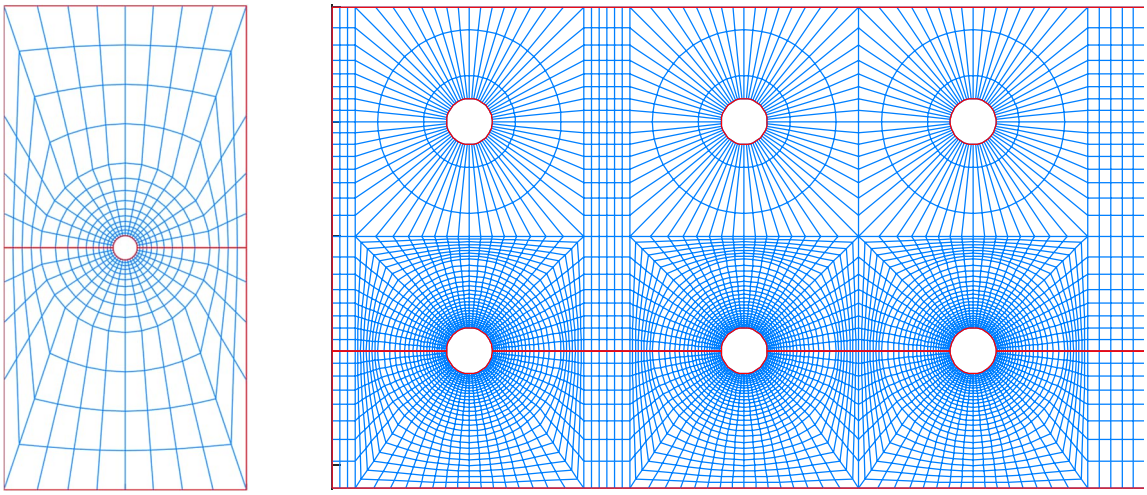

Figure 4.1-1. Mesh generated by the MATLAB program, for a single hole (left) and for multiple holes (right).

The user input also requires a pre-definition of the crack path. Along this path, the nodes of the neighboring elements are disconnected, as indicated by the horizontal red line emanating from the holes in Fig. 4.1-1. The FE-program utilizes first or second order isoparametric element formulations and allows for enforcement of single-point or multi-point constraints of degrees of freedom. Single-point constraints are used for definition of boundary conditions, while multi-point constraints control the opening and closing of the nodes along the crack path. The multi-point constraints are enforced by means of Lagrange multipliers. Loads can be applied on all unrestrained free boundaries.

Initially, all nodes along the crack path are closed to obtain the stress distribution for the uncracked configuration. After the initial solution, the crack size is increased incrementally by release of node pair constraints, according to a prescribed order, and the model is solved for each increment. Figure 4.1-2 shows an example of a stress plot of a solution for a two-row, ten-column joint with a long crack and fastener loads applied at all holes as bearing forces.

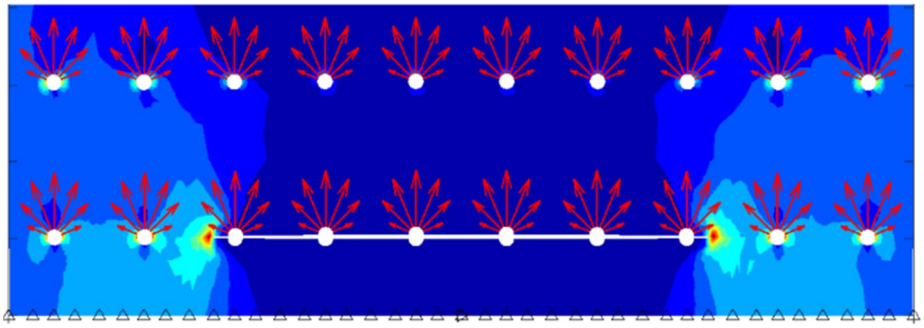

Figure 4.1-2. FE-model of crack growth in a joint.

Two methods are combined to calculate the SIF, weight function (WF) method and virtual crack closure technique (VCCT). For crack lengths $a<0.11R$, where a is the crack length measured from the hole edge and R is the hole radius, WF solution is used together with the stress distribution in the uncracked configuration, otherwise VCCT is used. The reason for combining the two solutions is that WF is inaccurate for relatively long crack lengths and VCCT is inaccurate for small cracks. Once the SIF as a function of crack length is obtained, the fatigue crack growth rate law can be integrated to calculate the crack growth. Figure 4.1-3 shows crack growth curves for spectrum loading of the joint shown in Fig. 4.1-2 for different starting points of the primary crack.

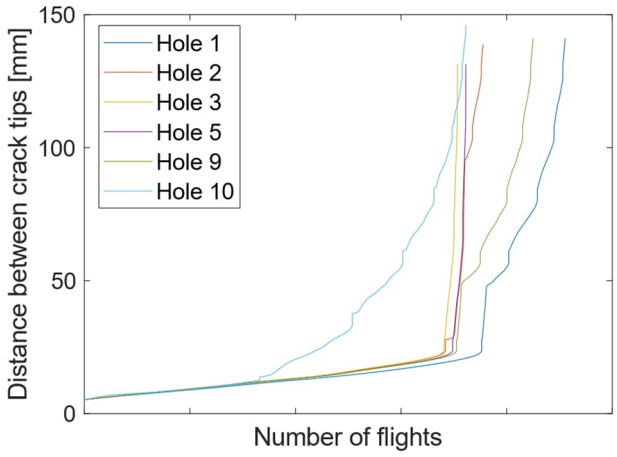

Figure 4.1-3. Crack growth for different starting points of the primary crack in the joint shown in Fig. 4.1-2.

Results and conclusion

In [1] the obtained solution is first validated for simple cases with one or several holes, with single or double cracks for by-pass and bearing loading. An example of comparison of the geometry function (normalized SIF) for the open-hole tension plate, between the current solution and a reference solution is shown in Fig. 4.1-4.

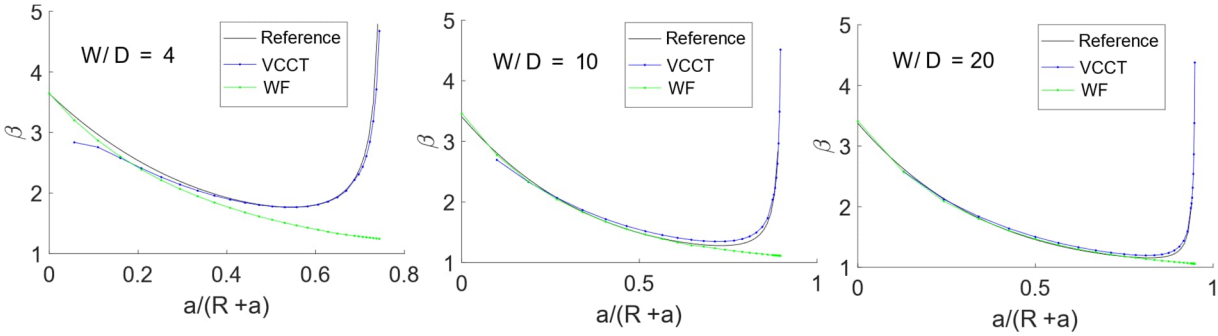

Figure 4.1-4. Comparison of geometry function for a double-crack in open-hole tension with three different width-to-diameter ratios, between a reference solution, VCCT-solution and WF solution.

In reference [1], several other validation and application cases are presented and discussed, as well as a number of convergence and parametric studies. At this stage of the program development, the mesh function is restricted to straight bolt rows but can easily be expanded to more general hole patterns and crack paths. Even so, the advantages of the FE-program are considerable. It can account for the effect of the neighboring holes, different applied and fastener load distributions and different fastener hole placements.

References

[1] E. Fernandez Rodriguez. Modelling of crack growth in structural joints. Master's Thesis, Linköping University, LIU-IEI-TEK-A–23/04510–SE, 2023.

4.2 Round robin stress intensity factor benchmark

B. Andersson[1], *R. Pilarczyk*[2], *J. Guymon*[2]

[1]BARE AB, Västerås, Sweden,
[2]Hill Engineering, Marriott-Slaterville, UT, USA

Below we summarize results from a recent benchmark study "Stress Intensity K_I Comparison Round Robin" executed 2021-2022 [1]. The study was launched by the Engineered Residual Stress Implementation (ERSI) working group.
The background is that in 2017, a "Fatigue Crack Growth (FCG) Analysis Methods" round robin was completed with the objective to quantify the crack growth life for cold expanded fastener holes. During this round robin, some peculiar results found were judged to be the result of errors in K_I-solutions, however other factors could also had been contributing. As the extent of the error was unclear, further work was deemed necessary to quantify any error or discrepancy in the K_I-solutions.
As a result of these findings a follow-on collaborative round robin was established, the one summarized here, to investigate differences in stress intensity factors readily available in commercial software like AFGROW and NASGRO.
Benchmark objectives. The primary objective of the Stress Intensity Factor (K_I) round robin was to evaluate differences between available K_I-solutions for a single corner crack at a fastener hole with remote uniform tension loading. The evaluations included effects single versus double cracks, finite width, and hole offset. These solutions were compared to explicit Finite Element Analysis (FEM) results of each case. Any findings were intended to drive improvements to solutions available to the fracture community.

Overview of benchmark cases

The present round robin considered seven different cases of corner crack(s) at a hole in a rectangular plate, see Figure 4.2-1. Calculated $K_I(\phi)$-solutions along the crack front ($0 \leq \phi \leq \pi/2$) were requested from the eight participants in this blind test. A building block approach was utilized when setting up the seven benchmark cases in order to understand the influence of various factors. Table 4.2-1 provides an overview of the seven cases evaluated for the round robin. Case 1 represents the reference solution, without any corrections for single cracks, finite width, hole offset or crack aspect ratio. The Poisson's ratio used in all analyzes is 0.30.

Table 4.2-1. Summary of Round Robin Cases

Case	***Cracks***	***W/D***	***a/t***	***a/c***	***Offset/W***
1	2	200	0.1	1	0.5
2	1	200	0.1	1	0.5
3	1	8	0.1	1	0.5
4	1	8	0.1	1	**0.15**
5	1	**2.4**	0.1	1	0.5
6	1	200	0.2	1.5	0.5
7	1	200	0.2	0.5	0.5

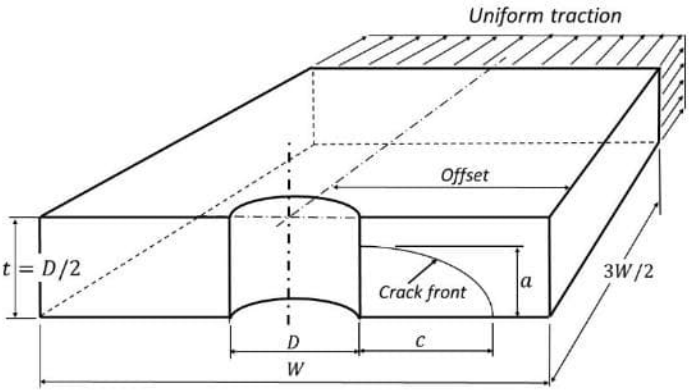

Figure 4.2-1. Round robin domain (half domain is shown) with single corner crack at a straight shank hole. The 'Offset' shown is the distance from hole center to the right specimen surface.

Round robin contributors and analysis techniques used

Table 4.2-1 provides a matrix of all submissions and analysis techniques used. There were three software companies which used the FEM-software StressCheck, Marc and SimModeler respectively to analyze Cases 1 to 7. Two software designed for fatigue crack growth predictions, namely AFGROW and NASGRO were also used. Classical Newman-Raju semi-analytic approach, including recent developments (by J. Newman [1]) were also included in the study. An USAF contractor, BARE, employed a hp-version of the finite element method and derived (Submission #6) highly accurate reference solutions to Cases 1 to 7 to be used as reference in the blind test. Each of these solutions had a relative error in K_I of less than 0.03% at arbitrary points ϕ along the entire crack front (including the vertex regions where $K_I \to 0$).

Benchmark results

Figure 4.2-2 exemplifies the relative error in $K_I(\phi)$ in the range $0 \le \phi \le \pi/2$ for Case 1 for all submissions. The figure shows that all submissions, that is FEM-solutions, AFGROW and NASGRO and the semi-analytic Newman-Raju method all gives small errors within +/- 2% except very close to the two vertices where the errors go to infinity as the reference solutions have $K_I \to 0$ at the vertices.
Table 4.2-3 which gives an overview of all benchmark results shows the obtained error ranges for Case 1 to 7 and all submissions. The table shows that the errors in the three different FEM-solutions are small for Cases 1-7 for practical purposes. An error of 2% in K_I through-out an entire fatigue crack growth analysis would typically result in an error of 10% in predicted fatigue life, except for load spectra which leads to low K_I-values close to threshold values. The errors are also small for Case 1, 2, 3, 6 and 7 in all submissions.
The only cases of concern are Cases 4 and 5 (highlighted in red color in the table) for a few submissions. The large errors for Case 4 shows that the two functions used for compensating for offset in AFGROW, NASGRO and the NR-solutions is not very accurate (the techniques used are listed in Table 4.2-2). For case 5, that is the narrow plate with W/D=2.4, AFGROW and the Newman-Raju solutions are very large in error.

Table 4.2-2: Summary of submissions and techniques used in the benchmark. Submission #5 has intentionally been left out from the present summary.

Sub-mission #	Title	SIF solution source	Single Corner Crack	Finite Width	Offset Hole
Case	**-**	**-**	**2-7**	**3-5**	**4**
#1	Fawaz-Andersson Solutions, AFGROW	Fawaz-Andersson [2] (as implemented in AFGROW Advanced Model)	n/a	Newman [5]	Harter [3]
#2	Newman-Raju Fit to Fawaz-Andersson	Updated equations by Newman [4] based on fit to Fawaz-Andersson solutions [2]	Shah-Newman [1]	Newman [5]	Kt match approach
#3	Newman-Raju (1986)	1986 Newman-Raju solution [5]	Shah correction	Newman [5]	Kt match approach
#4	NASGRO (CC16): Fawaz-Andersson	Fawaz-Andersson solutions [2] (as implemented in NASGRO CC16)	n/a	Modified version [9] of the Newman correction [5]	Harter [3] (as impl. in NASGRO CC16)
#6	Andersson: FEA (2021)	Explicitly modeled each condition utilizing the STRIPE FE-software for the *hp*-version of the finite element method			
#7	SimModeler Crack: FEA (2021)	Utilized SimModeler Crack to create 3D FEMs and compute K_I via displacement correlation technique [9]			
#8	StressCheck: FEA (2021)	Utilized StressCheck to compute K_I [8]			
#9	Marc: FEA (2021)	Utilized Marc to create 3D FEMs and compute K_I			

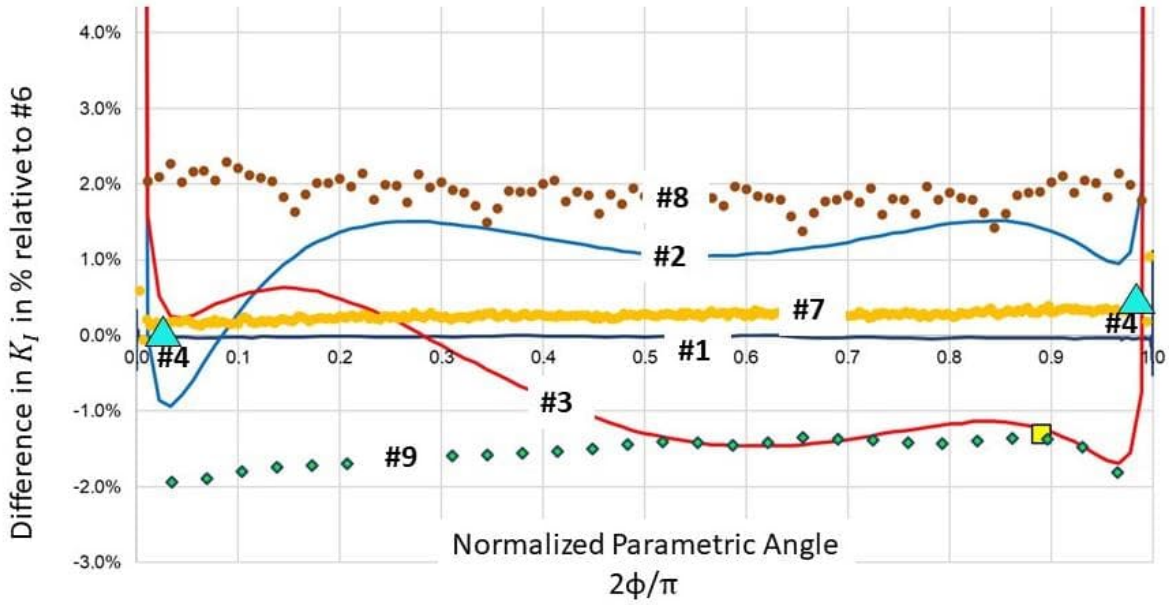

Figure 4.2-2. Relative errors in $K_I(\phi)$ for Case 1 and all submissions.

Table 4.2-3: Error range in K_I for Case 1 to 7 and all submissions (the close vertex regions are excluded).

Case	FEM-solutions	AFGROW	NASGRO	NR-solution
1	-2% to +2%	~0	0% to 0.5%	-1% to 2%
2	-1% to +2%	~0	-0.5% to 0%	-0.5% to 2%
3	-1% to +2%	-0.6%	-0.5% to -0.2%	-1% to 2%
4	-2% to +2%	-4.5% to -2%	+3.0% to +3.5%	-6% to -3%
5	-1% to +2%	-8% to -7%	-2%	-8% to -5%
6	-2% to +2%	~0	-2% to 0%	-2% to 2%
7	-2% to +3%	~0	~0	-2% to +1%

Follow-on investigations

Three round robin partners performed additional K_I-convergence studies which are reported in detail in the final report [1] and in greatest detail in an accompanying Excel sheet [11]. Additional studies of finite width correction function were also initiated during the benchmark period. A study 2022 resulting in 86000 highly accurate plate analyses (relative error of order 0.03% along the entire crack fronts) covering a large $K_I(D/t, W/D, a/t, a/c)$-space for tension, bending and pin loading [10]. These solutions have been delivered to AFGROW- and NASGRO-developers during 2023.

Overall summary and conclusions

- Successful SIF K_I comparisons were completed utilizing an array of available solutions and toolsets, with submissions provided by 8 different participants
- Overall, results were within 2% of the reference case, however, significant deviations were observed for the narrow width specimen leading to errors of up to 10%. Data in [10] which have been delivered to AFGROW and NASGRO groups covers completely the lack of data that existed at start of the benchmark
- Analysts wanting to use the closed form equation approach should strongly consider using the "Shah-Newman correction (2020)" [1] to correct for a single crack from a double symmetric crack
- A robust dataset, available as an Excel sheet [11], was developed that can be utilized as a reference set for follow-on studies
- More round robin challenges should be considered for advancing the knowledge of the entire damage tolerance design community. Simple geometries with more complex loading conditions as well as component level geometries should be considered in future challenges.

References

[1] R. Pilarczyk, J. Guymon, et al. Engineered Residual Stress Implementation (ERSI) Stress Intensity Comparisons Round Robin. Report Number ERSI-2021-01, Revision IR, 6 June 2022, https://residualstress.org/images/9/92/ERSI-2021-01_Stress_Intensity_Comparison_Round_Robin_-_Report_%26_Data.pdf

[2] S.A. Fawaz, B. Andersson. Accurate stress intensity factor solutions for corner cracks at a hole. Engineering Fracture Mechanics 71(9) (2004) 1235-1254.

[3] J. Harter. AFGROW User's Guide and Technical Manual, Version 5.3, Section 3.2.3.1.1.5.

<https://afgrow.net/DocumentHandler.ashx?name=AFGROW_Technical_Manual_and_Users_Guide_5-3-5-24.pdf>
[4] J.C. Newman Jr. Evaluation of Structural Integrity Analysis Methodologies for Corrosion Prediction Models. Final Report S&K Technologies, Inc., July 2005 (Revision June 2012).
[5] J. C. Newman Jr., I. S. Raju. Stress-intensity Factor Equations for Cracks in Three-Dimensional Finite Bodies Subjected to Tension and Bending Loads. Computational Methods in the Mechanics of Fracture, Vol. 2, S. N. Atluri (ed.), 1986, pp. 311-334.
[6] R.C. Shah. Stress Intensity Factors for Through and Part-Through Cracks Originating at Fastener Holes. In: J.R. Rice, P.C. Paris (Eds.), ASTM International, West Conshohocken, PA, 1976, pp. 429-459.
[7] Y. J. Guo. Finite width correction and hole offset correction for one corner crack at an offset hole in a finite plate. NASGRO, Houston, TX, USA, Tech. Rep. Internal, 2013.
[8] https://www.esrd.com/product/computation-of-sifs-in-stresscheck/
[9] A. Loghin. Quantification of the Impact of the Crack Shape Constraint Assumptions onto Predicted Remaining Useful Life. ASME Turbo Expo 2022 Proceedings, GT2022-80229.
[10] B. Andersson. $K_I(\phi)$-Databases for a Single Crack at a Straight Shank Hole in Plates of Variable Width. Report BARE, 29 Nov 2022, 11 pp.
[11] https://residualstress.org/images/c/c3/SIF_Round_Robin_Data_Summary_r0vf.xlsx

4.3 $K_I(\phi)$ – databases for a single crack at a countersunk hole in plates of variable width

B. Andersson[1]

[1]BARE AB, Västerås, Sweden

The USAFA contractor BARE provides since 2002 stress intensity functions $K_I(\phi)$ data which are implemented in the commercially available AFGROW and NASGRO fatigue crack growth analysis codes [1]. The ERSI benchmark executed 2022, see [2], emphasized an urgent need for new and accurate K_I-data for specimens of narrow width as classical analytical expressions for "finite width corrections" used for decades lead to errors in K_I of up to 40% (Table 13 in [2]). The present summary describes newly developed K_I-data for single cracks at a countersunk hole for the load cases tension, bending and pin loading, respectively [3]. The total number of new and very accurate K_I-functions is about 110*k* (thousand). At about 38% of the investigated 220*k* crack vertices do K_I go to infinity, something that pose difficulties in the numerical analysis as well as introduces the technical difficulty of how to use these data in a fatigue crack growth analysis. The delivered K_I-data to AFGROW and NASGRO groups have near each crack vertex been analyzed by using the mathematical vertex theory described in [3]. 220*k* high accuracy *analytical* formulas for K_I have been created. These analytic formulas can be used to calculate K_I near, and at arbitrary small distances from the actual vertex.
Figure 4.3-1 shows the plate dimensions $(2 \cdot W, 6 \cdot W, t)$ and the crack size (quarter-elliptical crack with axes (a, c)) considered in the developed databases. The stress intensity functions $K_I(\phi)$ are independent of the modulus of elasticity but depends on the Poisson's ratio ν. A value of ν=0.3 was used in all analyzes. Figure 4.3-2 shows schematically the three loading cases considered for each specimen and crack geometry. The stress intensity functions $K_I(\phi)$ for tension, bending and pin loading which are given in all databases refer to the load systems shown in Figure 4.3-2.

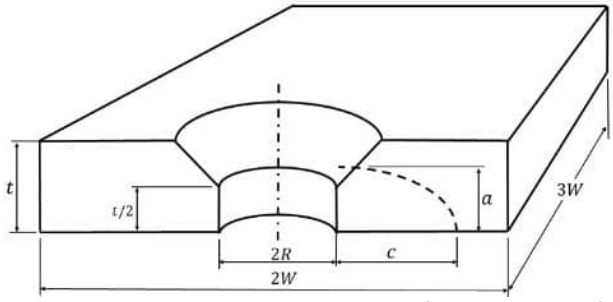

Figure 4.3-1. Single crack scenario in plate with dimensions $(2 \cdot W, 6 \cdot W, t)$ where the single crack of size (a, c) satisfying $c + R \leq W$ and $0.1 \leq \frac{a}{t} \leq 15$. The countersunk angle is 100^o.

The pin loading case used that is the function $Q(x, r, \varphi)$ requires a definition. $Q(x, r, \varphi)$ is a traction load acting in the radial (r) direction on a part, i.e. $-90^o \leq \varphi \leq 90^o$, of the cylindrical and conical hole surfaces. The angle φ is zero at the vertical line through the center of the hole (see Figure 4.3-2, right part). The 2019 years pin-load model developed by BARE was used in all analyzes. The advantages of using this model are described in [4].

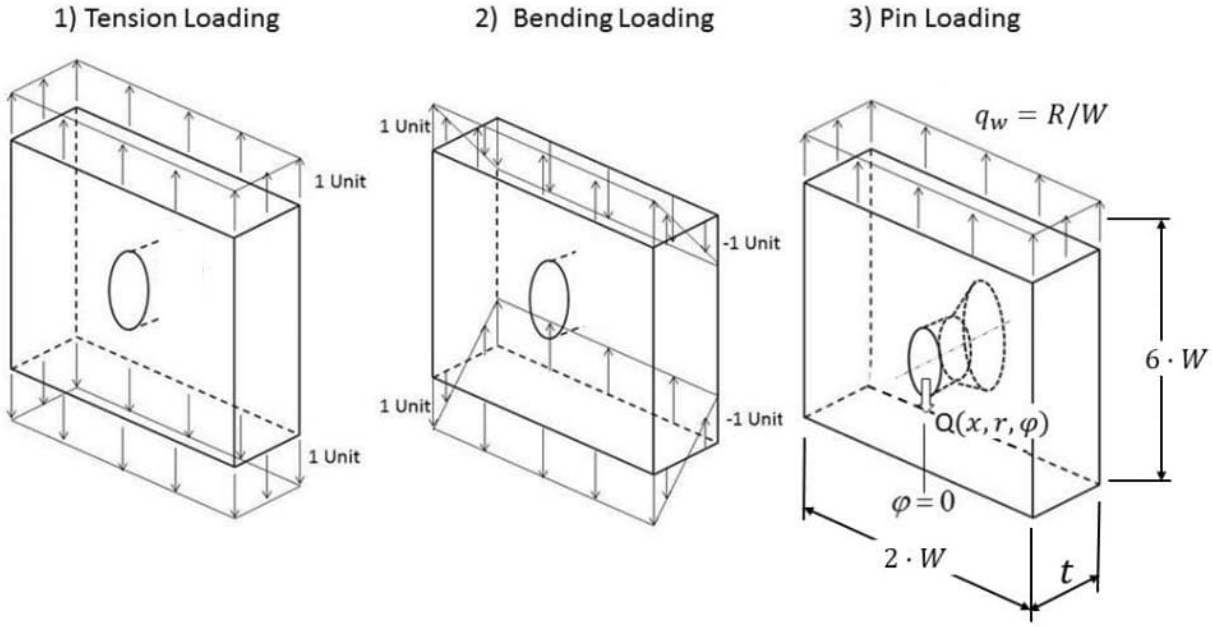

Figure 4.3-2. Basic load cases acting on a plate with dimensions $(2 \cdot W, 6 \cdot W, t)$.

The created data bases cover the following parameters, that is, 8 $\left(\frac{R}{t}\right)$-values, 20 $\left(\frac{c}{a}\right)$-values, 20 $\left(\frac{a}{t}\right)$-values and 19 $\left(\frac{W}{R}\right)$-values for the three loading cases.

$a/c =$ 0.10, 0.125, 0.1667, 0.20, 0.25, 0.333, 0.5000, 0.667,
0.75, 0.800, 0.900, 1.000, 1.111, 1.25, 1.333, 1.500,
2.00, 3.00, 6.00, 10.00. eq. 1

a/t= 0.1, 0.2, 0.3, 0.4, 0.5, 0.6, 0.7, 0.8, 0.9, 0.95, 1.10,
1.25, 1.4, 1.8, 2.4, 3.2, 4.5, 6.5, 10.0, 15.0 eq. 2

R/t = 0.2, 0.333, 0.5, 1.0, 1.5, 2.0, 3.0, 5.0 eq. 3

$W/R =$ 2.4, 2.6, 2.8, 3.2, 3.6, 4.0, 4.6, 5.2,
5.8, 6.4, 7.0, 8.0, 9.0, 10.0, 12.0, 16.0,
20.0, 30.0, 40.0 eq. 4

FEM-meshes used in all analyzes are designed for the *hp*-version of FEM. The relative errors in calculated stress intensity functions $K_I(\phi)$ are very small, that is lower than 0.05%. This also includes arbitrary small distance from the crack vertices.

Accurate determination of $K_I(\phi)$ near vertices

The fact that K_I goes to infinity at 38% of the investigated vertices needs special attention. Figure 4.3-3 exemplifies cracks of various sizes in countersunk hole geometries studied. $K_I(\phi)$ is near each of the six vertices v_i given by the following expression,

$$K(s) = \sum_{I=0}^{I=\infty} \sum_{i=1}^{i=\infty} S_{i,I} \cdot s^{\Lambda_i - 1/2 + I} \qquad \text{eq. 5}$$

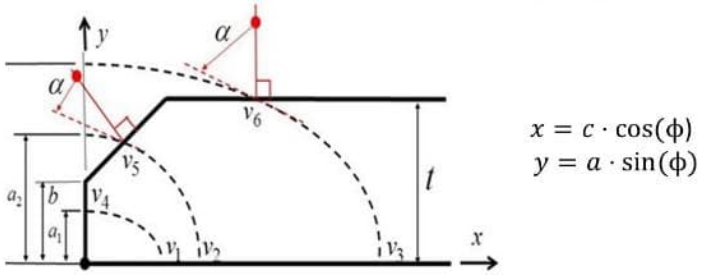

Figure 4.3-3. Three crack sizes with six vertices $v_1,\ v_2, \ldots v_6$ of interest.

In equation (5), $S_{\{i,I\}}$ are unknown constants, which we label *vertex* intensity factors, $\Lambda_i(\alpha)$ constants, that are computed with the BARE software STRIPE, and $s(\phi)$ the crack front arc length. The vertex singularities $\Lambda_i(\alpha)$ depends only on Poisson's ratio.

The angle α depends on the geometrical factors (c, a, b, t) determines if $\Lambda_1$is smaller or larger than ½, that is, if K_I will go to zero or infinity at the vertex considered (compare (5)). We have for the 220*k* crack vertices considered determined the unknown constants $S_{i,I}$ in such a way that Eq. 5 is in closest possible agreement with the available finite element solutions for K_I over a part of the crack front. Reference [3] provides more details.

The accuracy of (5) have been checked by inspecting 23k plots of the type shown in Figure 4.3-4. The table to left lists all *W/R*-values for which *K*-solutions are available. In the same table we have listed the error in the least square approximation in the actual crack front region used. We see that the average error is very small (less than 0.02%) in all 19 *K*-functions shown. The joint geometry and the crack front (red color) is also shown (in scale, save for the hole radius *R*=10) in upper part of the figure. The two blue dots on the (red) crack front marks the region used when doing the least square fit. The blue dots are also marked on each K-curve.

The figure shows that the 'a'-vertex is located on the upper plate surface and that the tangent to the crack front forms an angle $\alpha = 63.4^o$with the normal to the plate surface. Such large α-angles gives very low Λ_1-values (Λ_1=0.2824) that is $K_I(\phi)$ goes to infinity asymptotically as $s^{-0.2176}$, *s* being the distance to the vertex. The finite element *K*-solutions are represented by the small black disks and the red curves are the semi-analytic expression eq. 5 using four terms in the series. We note that also outside the range used for the least square fit do the small black disks fall 'exactly' on the red curves which verifies the mathematical vertex theory. In the delivered data bases with stress intensity *K*-data, the semi-analytic expression eq. 5 has been used to calculate K 'near' the two vertices. By 'near' we mean all points in the range used for the least square fit, and, all other points closer to the actual vertex. Hence, one can safely assume that the error in *K* arbitrary close to any of the 220*k* vertices is of order 0.05% or less. The first four vertex intensity factors S_i and the corresponding Λ-values are also available in data bases so the user of the data can compute *K* at arbitrary (small to medium) distances from the vertices.

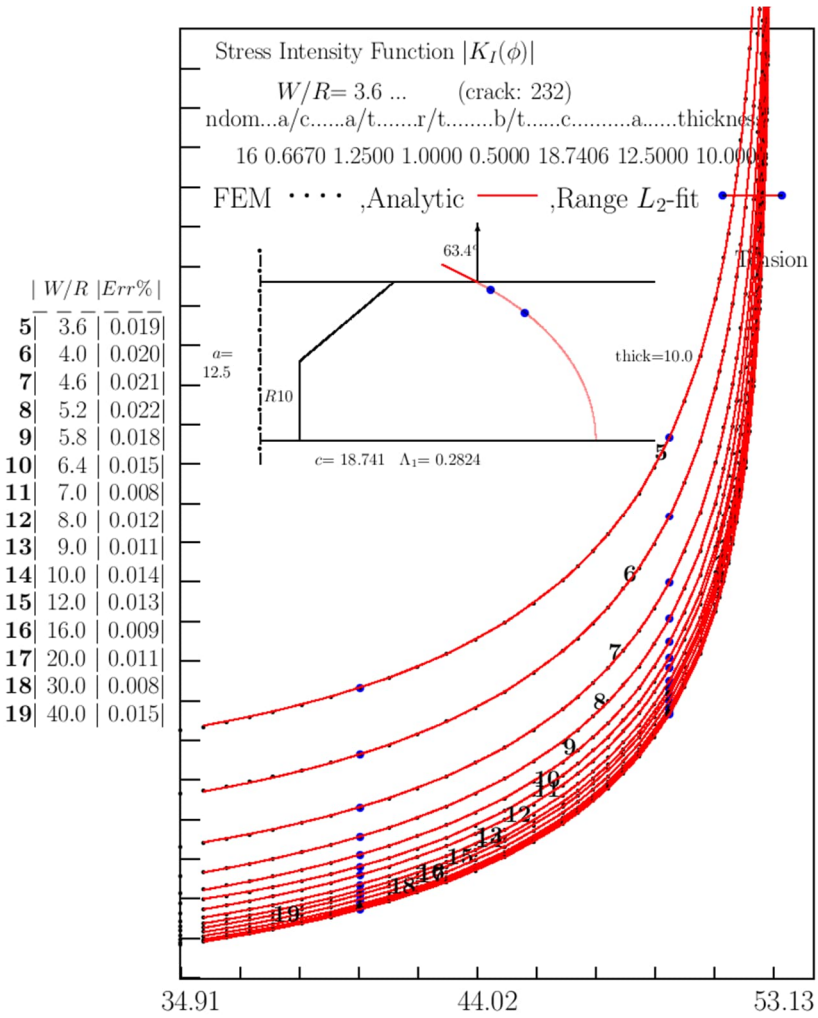

Figure 4.3-4. $K_I(\phi, W/R)$ near vertex 'a' ($\phi \approx 53.13^o$) for *R/t*=1 and *a/t*=1.25 and for *W/R*=3.6 ... 40.0.

Summary

Stress intensity functions have been calculated in a large parameter space for three loading cases. The relative error in all *K*-solutions are less than 0.05%. Closed-form expressions for *K* near all vertices have been extracted from the finite element solutions.About 23 thousand control diagrams are available for end users of the *K*- and *S*-databases generated. Data has been delivered to AFGROW and NASGRO groups.

References

[1] B. Andersson and J. Greer. Creation and Verification of World's largest K_I-Databases for Multiple Cracks at a Countersunk and Straight-Shank Hole in a Plate subject to Tension, Bending and Pin-Loading. 29'th ICAF Symposium, Nagoya, 7-9 June 2019, 10 pp.

[2] R. Pilarczyk, J. Guymon, et al. Engineered Residual Stress Implementation (ERSI) Stress Intensity Comparisons Round Robin. Report Number ERSI-2021-01, Revision IR, 6 June 2022, https://residualstress.org/images/9/92/ERSI-2021-01_Stress_Intensity_Comparison_Round_Robin_-_Report_%26_Data.pdf

[3] B. Andersson. $K_I(\phi)$-Databases for a Single Crack at a Countersunk Hole on Plates of Variable Width. BARE report 28 Feb 2023, 10 pp.

[4] B. Andersson. A Pin-Load Model for Worst Scenario $K_I(\phi)$-Analysis. AFGROW User Work Shop, Layton UT, Sept 14-15, 2020, 23 pp.

4.4 $K_I(\phi)$ – databases for a single crack at a straight shank hole in plates of variable width

B. Andersson[1]

[1]BARE AB, Västerås, Sweden

The ERSI benchmark executed 2022, see [1], emphasized an urgent need for new and accurate K_I-data for specimens of narrow width as classical analytical expressions for "finite width corrections" used for decades lead to errors in K_I of up to 40% (Table 13 in [1]). BARE did therefore during 2022 derive 27 new $K_I(\phi)$ -databases valid for a single crack at a straight-shank hole in a plate subject to tension, bending and pin loading. The total number of new and very accurate K_I-functions in this effort is about 258*k* (thousand). These data have been delivered to developers of the AFGROW and NASGRO fatigue crack growth analysis codes. The delivered K_I-data have near each crack vertex been analyzed by using the mathematical vertex theory described in [2]. 516*k* high accuracy *analytical* formulas for K_I have been created. These analytic formulas can be used to calculate K_I near, and at arbitrary small distances from the actual vertex.

Figure 4.4-1 shows the plate dimensions considered $(2 \cdot W, 10 \cdot W, t)$ and the crack size (quarter-elliptical crack with axes (a, c)) in the developed databases. Previously available databases from 2003 and 2017 had fixed $\frac{W}{R} = 100$ and $\frac{W}{t} = 100$, respectively.

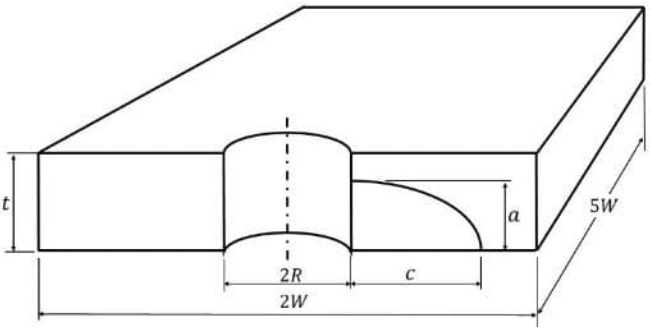

Figure 4.4-1. Single crack scenario in plate with dimensions $(2 \cdot W, 10 \cdot W, t)$ where the single crack of size (a, c) satisfies $a < t, c + R \leq W$.

The stress intensity functions $K_I(\phi)$ are independent of the modulus of elasticity but depends on the Poisson's ratio ν. A value of ν=0.3 was used in all analyzes. Figure 4.4-2 shows schematically the three loading cases analyzed for each specimen and crack geometry. The stress intensity functions $K_I(\phi)$ for tension, bending and pin loading which are given in all databases refer to the load systems in Figure 4.4-2.

$Q(\varphi)$ (Figure 4.4-2) is a traction load acting perpendicular to the hole surface. $Q(\varphi)$ is the load intensity, which is uniform in the thickness direction. We used,

$$Q(\varphi) = \begin{Bmatrix} q \cdot \cos^2(\varphi) & \text{for} & -\pi/2 \leq \varphi \leq \pi/2 \\ 0 & \text{for} & |\varphi| > \pi/2 \end{Bmatrix} \qquad \text{(eq.1)}$$

The total force acting on the upper plate surface is $F = 2 \cdot W \cdot t$ which gives

$$q = \frac{3 \cdot W}{2 \cdot R} \qquad \text{(eq. 2)}$$

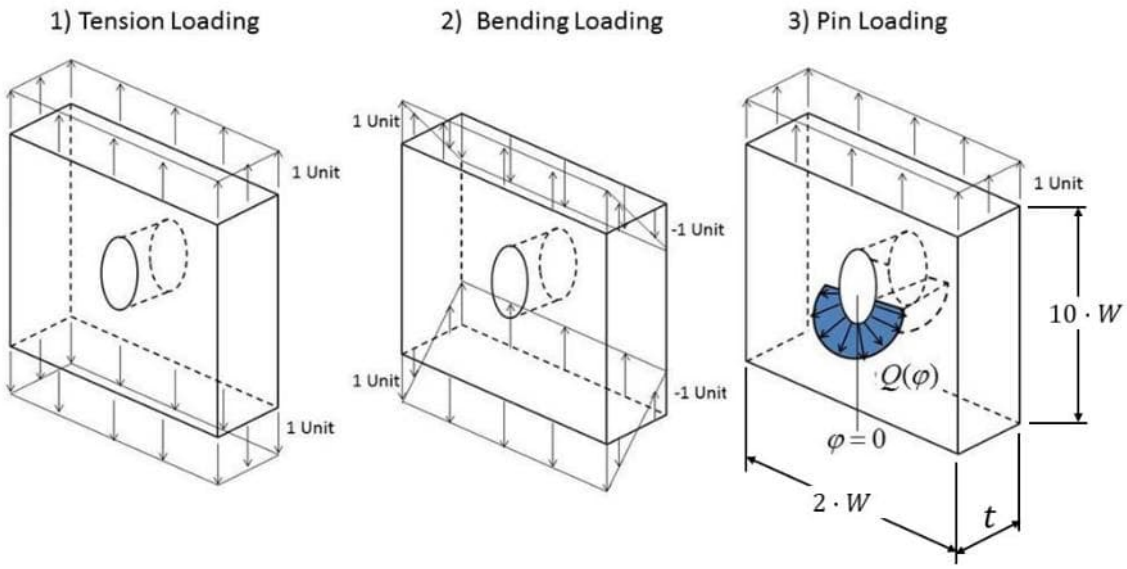

Figure 4.4-2. Basic load cases acting on plate with dimensions $(2 \cdot W, 10 \cdot W, t)$.

In the finite element analysis, a user-supplied subroutine calculates the tractions in Gaussian points for pin loading from eq. 1 and eq. 2.

The created data bases cover the following parameters, that is 27 $\left(\frac{R}{t}\right)$-values, 25 $\left(\frac{c}{a}\right)$-values, 10 $\left(\frac{a}{t}\right)$-values and 18 $\left(\frac{W}{R}\right)$-values for the three loading cases.

$c/a =$ 0.10, 0.111, 0.125, 0.1428, 0.1667, 0.20, 0.25, 0.333, 0.5000, 0.667, 0.800, 0.900, 1.000, 1.25, 1.333, 1.500, 2.00, 2.25, 2.50, 3.000, 4.00, 5.00, 6.00, 8.00, 10.00. (eq. 3)

$a/t =$ 0.10, 0.20, 0.30, 0.40, 0.50, 0.60, 0.70, 0.80, 0.90, 0.95 (eq. 4)

R/t = 0.1, 0.125, 0.1428, 0.1667, 0.2, 0.25, 0.333, 0.4, 0.4444, 0.5, 0.5714, 0.667, 0.8, 1.0, 1.25, 1.5, 1.75, 2.0, 2.25, 2.5, 3.0, 4.0, 5.0, 6.0, 7.0, 8.0,10.0 (eq. 5)

$W/R =$ 1.6, 1.8, 2.0, 2.2, 2.4, 2.8, 3.2, 3.6, 4.0, 4.6, 5.2, 5.8, 6.4, 7.0, 8.0, 10.0, 12.0, 15.0 (eq. 6)

FE-meshes used are designed for the *hp*-version of FEM. The relative errors in calculated stress intensity functions $K_I(\phi)$ are very small, that is typically less than 0.05%.

All elliptical crack fronts considered intersect at right angles with the free plate surfaces. This implies that the stress intensity factors are zero at all vertices. The mathematical vertex theory can be used to obtain closed-form analytic expressions for $K_I(\phi)$ near any vertex. The closed form solution can be written as,

$$K(s) = \sum_{I=0}^{I=\infty} \sum_{i=1}^{i=\infty} S_{i,I} \cdot s^{\Lambda_i - 1/2 + I} \quad \text{(eq. 7)}$$

$S_{i,I}$ are unknown constants so called *Vertex* stress intensity factors, Λ_i known constants that have been computed with the BARE software STRIPE. The function $s(\phi)$ in eq. 7 is the crack

front arc length measured from the actual vertex. The coefficients Λ_i depends only on Poisson's ratio for the material. BARE has computed the first four coefficients $S_{i,I}$ in eq. 7 for each plate, each crack vertex and each load case in the database. The coefficients were determined by doing a least square fit of eq. 7 to *K*-data obtained from the FEM-solutions. Four coefficients are enough to get a very accurate closed form expression for *K* in a very large region around the actual vertex.

The accuracy of the closed form approximation is checked by plotting equation eq. 7 together with the FE-solution (for all plates, vertices and load cases). Figure 4.4-3 exemplifies how well the closed form expression eq. 7 (red curves) fits actual FE-solutions (black dots) for 18 *W/R* values. The closed form expression eq.7 makes it possible to determine *K* arbitrary close to a vertex with a relative error less than estimated 0.03%.

Comparisons of the type shown in Figure 4.4-3 are, for each fixed *R/t*, checked for 250 crack sizes, 2 vertices and 3 load cases (1500 slides).

The final database aimed for end users of *K*-data consists of a combination of *K*-values from the FEM-analysis (away from vertices) and two closed form solutions eq. 7 (near the two vertices).

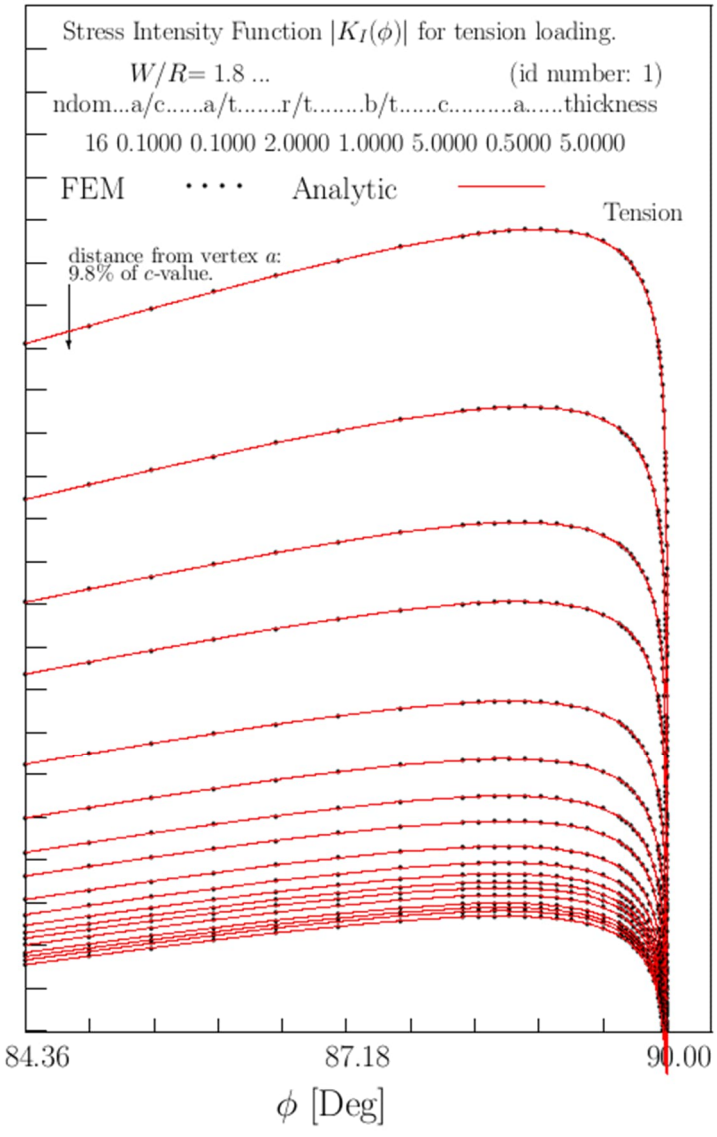

Figure 4.4-3. $K_I(\phi, W/R)$ near vertex 'a' ($\phi \approx 90^o$) for *R/t*=2 and *a/t*=0.1 and for *W/R*=1.8 ... 15.0.

Summary

Stress intensity functions have been calculated in a large parameter space for three loading cases. The relative error in all *K*-solutions are less than 0.05%. Closed-form expressions for *K* near all vertices have been extracted from the finite element solutions.

References

[1] R. Pilarczyk, J. Guymon, et al. Engineered Residual Stress Implementation (ERSI) Stress Intensity Comparisons Round Robin. Report Number ERSI-2021-01, Revision IR, 6 June 2022, https://residualstress.org/images/9/92/ERSI-2021-01_Stress_Intensity_Comparison_Round_Robin_-_Report_%26_Data.pdf

[2] B. Andersson. $K_I(\phi)$-Databases for a Single Crack at a Straight Shank Hole on Plates of Variable Width. BARE report 29 Nov 2023, 10 pp.

4.5 Continuous-time, high-cycle fatigue modelling of aluminum structure

Z. Kapidzic[1], *S. B. Lindström*[2]

[1]Saab Aeronautics, Linköping, Sweden,
[2]Mid Sweden University, Sundsvall, Sweden

Introduction

Development om machining technique during the last decades has made it feasible to manufacture components of aluminum airframe structure as large integral parts instead of traditionally joined structure. The advantages of integral structure are simplified assembly process, reduced number of parts and the possibility to integrate complex geometries and thereby facilitate weight reduction. The downside is that heavily integrated structures are difficult to inspect, repair or replace in case of fatigue damage or failure. Also, integral structure tends to have more complex geometry and is therefore also exposed to more complex loading history than traditionally built structure. Figure 4.5-1 shows an example of complex geometry in an integral aluminum frame structure.

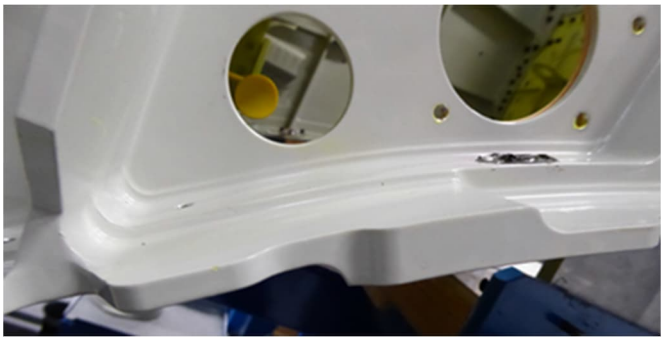

Figure 4.5-1. Detail of airframe structure.

As ever higher demands are placed on the efficiency and of integrated structures the demands for ability to assess the fatigue life increase. The fatigue assessment methods and models must be reliable and advanced enough in order to take into account the geometry, material and load complexities in integral structures. Traditional fatigue assessment methods, using cycle-counting methods, uniaxial stress assumptions and simple notch criteria may be oversimplifying and misleading in such cases.

To address this issue, Saab has together with Linköping University and Mid Sweden University developed a fatigue model that can take into account the complexities related to integral aluminum structure. The developed model is a continuation of work in [1] and is based on integration of continuous-time stress history and the concept of moving endurance surface in the stress space. This chapter briefly describes the basis of the model and two applications where the model has been implemented to solve plane problems with non-proportional loading [2] and three-dimensional problems with variable amplitude loading [3].

Fatigue model

The fatigue model considers a continuous-time stress history $\boldsymbol{\sigma}(t)$ that is calculated a *priori* using, *e.g.*, FE method for isotropic linear-elastic material behavior. The fatigue damage D is assumed to depend on the history of the first invariant $I_1 = tr(\boldsymbol{\sigma})$ and on the history of the equivalent stress $\bar{\sigma}(\boldsymbol{\sigma}, \boldsymbol{\alpha}) = \sqrt{3/2}\|\boldsymbol{s} - \boldsymbol{\alpha}\|$, where $\boldsymbol{\alpha}$ is a deviatoric backstress tensor. In order

to describe the evolution of the fatigue damage D over time, an endurance surface in the stress space is introduced, defined by the endurance function $\beta(\bar{\sigma}, I_1)$, so that $\beta(\bar{\sigma}, I_1) = 0$. The deviatoric backstress tensor $\boldsymbol{\alpha}$ is the center of the endurance surface in the deviatoric plane. Thus, the evolution of the backstress allows for the movement of the endurance surface. The fatigue damage parameter D that is initially equal to 0 and equal to 1 at fatigue failure. The evolution of the damage parameter and of the backstress are defined by the following rate equations

$$\dot{D} = \dot{\beta} g(\beta)$$
$$\dot{\boldsymbol{\alpha}} = \dot{\beta} C(\boldsymbol{s} - \boldsymbol{\alpha})$$

which are both non-zero only if $\beta \geq 0$ and $\dot{\beta} > 0$. In other words, the damage is developing and the endurance surface is moving only if the stress state is outside of the surface and moving away from it. In the above equations C is a material parameter and $g(\beta)$ is a damage function that is positive for $\beta \geq 0$. The above equations are integrated, using conventional methods, for any stress history thus eliminating the need for cycle counting.

The endurance function and the damage function need to be defined and several different functions have been proposed in the literature. Originally, in [1] a Drucker-Prager type of endurance function was suggested, while in [2] a quadratic function was used and in [3] a smooth step function was proposed for aluminum. Typically, the endurance function and the damage function contain parameters that need to be fitted to fatigue tests. In [3], a modification of the endurance and damage function parameters was suggested to account for notch effects, fatigue failure probability and surface conditions. The notch effect was introduced by letting $\beta(\bar{\sigma}, I_1, \chi)$, where χ is the relative stress gradient

$$\chi = \frac{\int_0^T |\nabla \sigma_{vM}| \, \|\dot{\boldsymbol{\sigma}}\| dt}{\int_0^T \sigma_{vM} \|\dot{\boldsymbol{\sigma}}\| \, dt}$$

and where σ_{vM} is the von-Mises stress. Thus, this modelling framework offers a capability to take into account various complex aspects fatigue of integral structure without any need for cycle counting, notch factor corrections or cumulative damage summation. It is also suitable for direct implementation in FE software.

Application to plane problems with non-proportional loading

Reference [2] presents and FE implementation of the proposed fatigue model to solve plane stress problems, including stress raisers, for applied non-proportional loading. The paper presents an example of a fatigue calculation on a web section of an integral fighter aircraft fuselage frame, see Fig. 4.5-2.

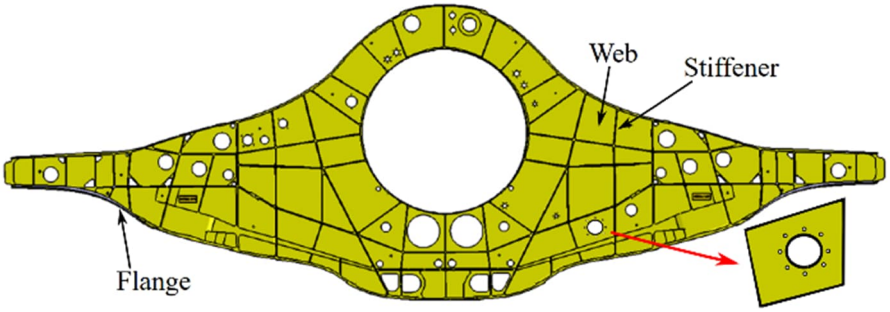

Figure 4.5-2. Integral frame geometry, figure from [2].

For the considered web section, indicated with the red arrow in Fig. 4.5-2, the in-plane load histories $N_{xx}(t)$, $N_{yy}(t)$ and $N_{xy}(t)$ are obtained as linear combinations of a large number load states which are solved by a global FE model of the whole aircraft. Figure 5.4-3 shows the global FE mesh and the applied in-plane loads on the web as well as their sequences.

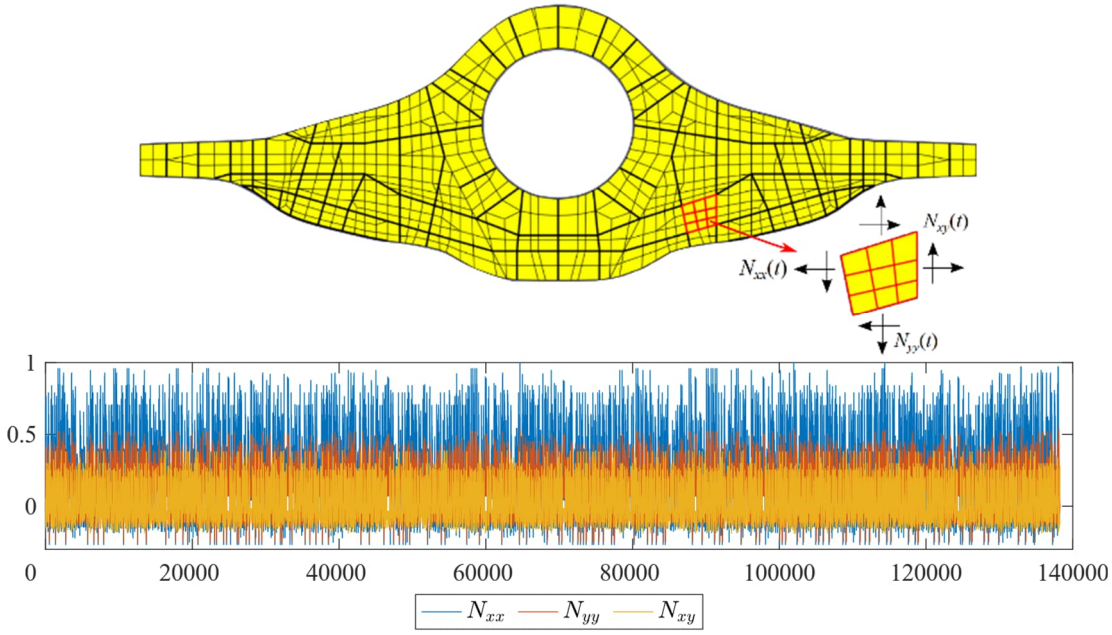

Figure 4.5-3. Global FE mesh of the frame and the in-plane load sequences, figure from [2].

Next, a local FE model of the web geometry including the stress raisers, is created in a MATLAB program and is solved for three unit load cases, one for each load component. The stress history is then obtained for all points on the edges of the stress raisers by superposition of the unit load case solutions. Finally, the fatigue damage is computed at all points on the edges of the stress raisers using the fatigue model. Figure 4.5-4 shows the local FE mesh of the web and the calculated damage along the hole edges for two loading scenarios.

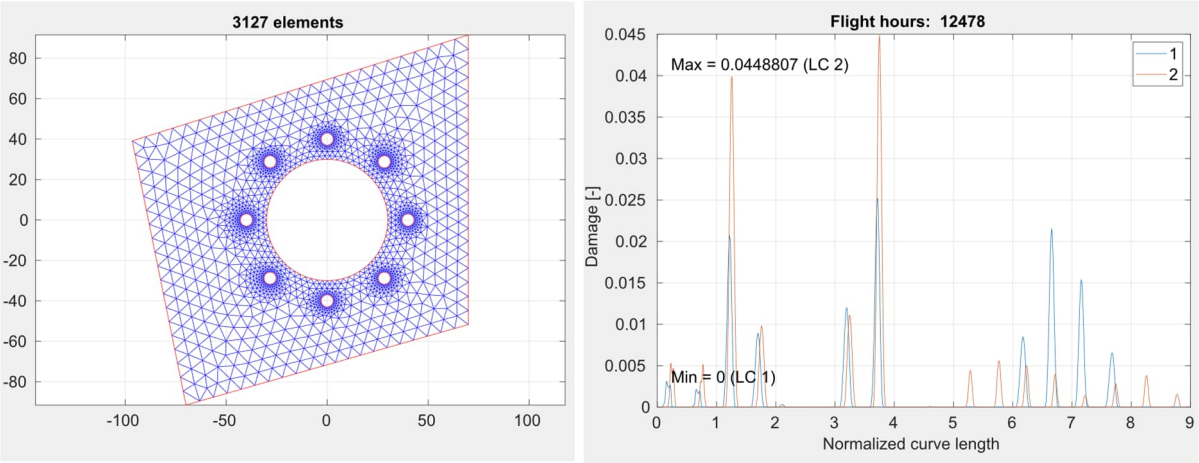

Figure 4.5-4. Local FE mesh of the web and the calculated damage along the normalized edge lengths, figure from [2].

The proposed fatigue model and the demonstrated implementation enable an efficient and automated process for the purpose of performing numerous calculation runs. The implemented tool is particularly useful for design of the placement and shape of the stress–raisers in plane aircraft frame structures.

Three-dimensional problems with variable amplitude loading

Reference [3] describes the proposed fatigue model in detail. It presents the results of constant amplitude tests performed on smooth and notched round specimens made of AA7050-T7451 and the procedure to fit the model parameters to the experimental data. Specifically, the modelling aspects regarding the fatigue failure probability and surface conditions are explained and exemplified. The fatigue model is implemented as a post-processing routine in the commercial software Abaqus. Given the unit load cases and their time-variation, the routine computes the stress variation and the number of cycles, or flights, to failure for a chosen number of nodes in the model.

Finally, the paper in [3] presents a verifying fatigue test and comparative calculation of fatigue life of a specimen with an airframe-like geometry made of AA7050-T7451. Figure 4.5-5 shows the 380 mm long specimen with pockets of different sizes and shapes, which contain thickness steps and radii. Such features are commonly found in integral frame structure, *cf.* Fig. 4.5-2. Twelve specimens were fatigue tested to failure by applying a variable amplitude force in the longitudinal direction of the specimen, using the Falstaff spectrum. The experimental results are compared to the fatigue life predictions in Fig. 4.5-6. Figure 4.5-7 shows an example of a plot of number of flights to failure for every node in the model and the location of the fatigue crack in the test specimens. The observed and predicted location of the fatigue crack initiation indicate the same point, as marked by a red arrow in Fig. 4.5-7.

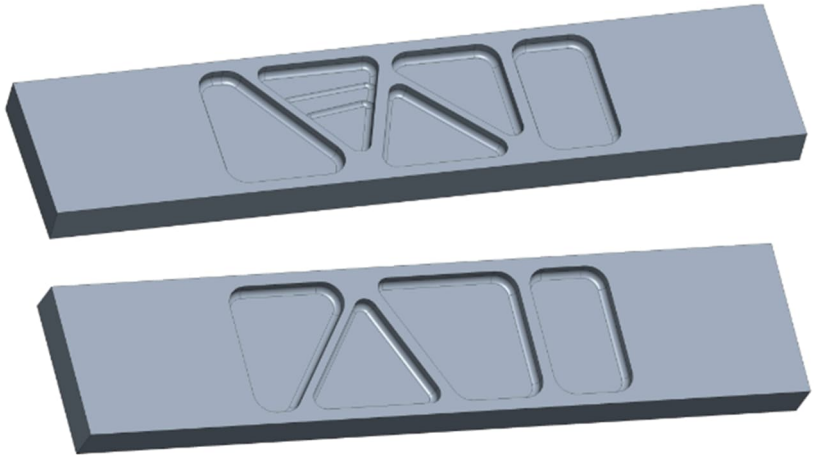

Figure 4.5-5. Specimen with airframe-like geometry, figure from [3].

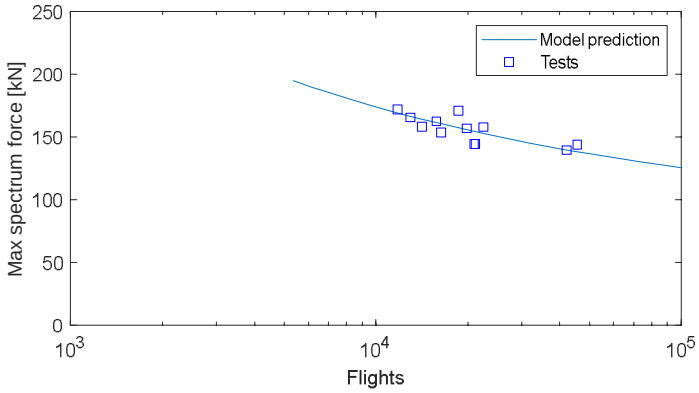

Figure 4.5-6. Comparison between the model prediction and test results, figure from [3].

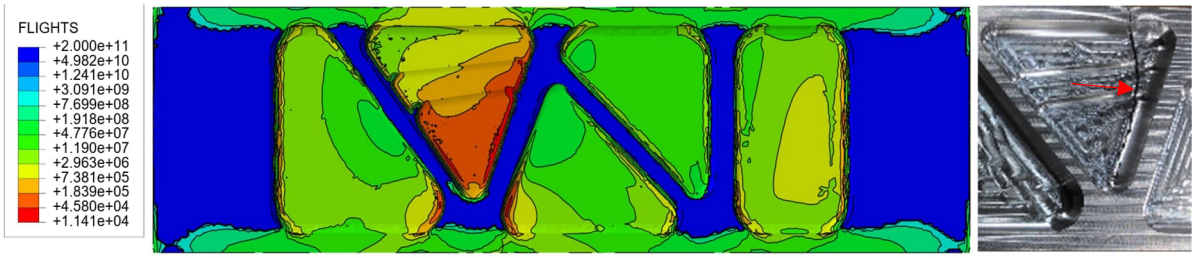

Figure 4.5-7. Predicted number of flights at maximum spectrum force 170 kN (left) and fatigue crack location in test (right), figure from [3].

The work was supported by the Swedish National Aeronautical Research Program 7 of Vinnova as grant agreement No. 2019-02778.

References

[1] N. S. Ottosen, R. Stenström, and M. Ristinmaa. Continuum approach to high-cycle fatigue modeling. International Journal of Fatigue, 30(6):996–1006, 2008.

[2] Z. Kapidžić, S. B. Lindström, J. Lundgren. Incremental fatigue damage model: Application to plane problems with non-proportional loading. 33rd Congress of International Council of the Aeronautical Sciences (ICAS), Stockholm, Sweden, 2022.

[3] S. B. Lindström, J. Moverare, J. Xu, D. Leidermark, R. Eriksson, H. Ansell, Z. Kapidžić. Service-life assessment of aircraft integral structures based on incremental fatigue damage modeling, International Journal of Fatigue, 172, 107600, 2023.

4.6 Topology optimization with a continuous-time, high-cycle fatigue constraint

S. Suresh[1], *S. B. Lindström*[2], *C-J. Thore*[1], *A. Klarbring*[1]

[1]Solid Mechanics, Linköping University, Linköping, Sweden**,**
[2]Mid Sweden University, Sundsvall, Sweden

Fatigue failure in mechanical components arises mainly due to fluctuating forces during the lifetime of a component. The modern use of integrated structural parts, to reduce the number of components, results in complex geometries making the fluctuating forces likely to be non-proportional. Therefore, to meet application demands, a high-cycle fatigue model that can handle proportional and non-proportional loads is required. Consequently, the continuous-time fatigue model by Ottosen *et al.* [1], [2] is used and the predicted damage is applied as a constraint in the topology optimization problems [3], [4]. This evolution-based model integrates the entire load history without using any cycle-counting algorithm for estimating the fatigue damage.

For a given stress history $\boldsymbol{\sigma}(t)$, the continuous-time fatigue model is based on the concept of an endurance surface $\{\boldsymbol{\sigma}|\beta(\boldsymbol{\sigma},\boldsymbol{\alpha}) = 0\}$, with $\boldsymbol{\alpha}$ as the back stress tensor and β as the endurance function. The damage is developed during the loading when $\beta > 0$ and $\dot{\beta} > 0$.

Lindström *et al.* [2] introduced a bivariate, quadratic polynomial endurance function. The purpose of this function is to enhance the accuracy and extrapolation capability of the original fatigue model by Ottosen *et al.* [1], particularly for non-proportional loads**.** The quadratic polynomial endurance function is defined as

$$\beta(\boldsymbol{\sigma},\boldsymbol{\alpha}) = \boldsymbol{y}^T\boldsymbol{A}\boldsymbol{y} + \boldsymbol{a}^T\boldsymbol{y} - 1$$

where $\boldsymbol{A}$ is a symmetric material parameter matrix, and $\boldsymbol{a}$ is a material parameter vector. The vector $\boldsymbol{y}$ reads $\boldsymbol{y} = \left[\frac{\bar{\sigma}}{E} \quad \frac{I_1}{E}\right]^T$, where E is the Young's modulus of the material, $I_1 = \mathrm{tr}(\boldsymbol{\sigma})$ and the effective stress $\bar{\sigma}$ is

$$\bar{\sigma} = \sqrt{\frac{3}{2}}\left|\left|\boldsymbol{s} - \boldsymbol{\alpha}\right|\right|$$

where $\boldsymbol{s}$ is the deviatoric stress tensor. The original continuous-time fatigue model in [1] emerges as a special case by setting $\boldsymbol{A} = \boldsymbol{0}$.

Two differential equations and their respective initial conditions govern the evolution of the back stress tensor $\boldsymbol{\alpha}$ and the fatigue damage D

$$\begin{aligned} \dot{\boldsymbol{\alpha}} &= C(\boldsymbol{s} - \boldsymbol{\alpha})\dot{\beta}, & \boldsymbol{\alpha}(0) &= \boldsymbol{0}, \\ \dot{D} &= K\exp(L\beta)\dot{\beta}, & D(0) &= 0 \end{aligned}$$

The fatigue damage $D(t)$ is a scalar-real value number that progressively increases from $D = 0$ (no damage) to $D = 1$ (critical failure). The set of above equation is integrated over the load history and thus not using any cycle counting algorithm. It also considers multi-axial and non-proportional stress states.

Utilizing the continuous-time fatigue model, a fatigue constraint is defined in a topology optimization problem. The design domain is discretized by the finite element method and each design variable x_e is associated to a finite element e. These design variables x should ideally take 0 (no material) or 1 (material).

To ensure a minimum life for the body, a single fatigue constraint evaluated at the final time $T = t_N = N\Delta t$, by means of P-norm reads

$$D^{PN}(\boldsymbol{x}) = \left[\sum_{e=1}^{n_e} D_{N,e}(\boldsymbol{x})^P\right]^{\frac{1}{P}} \leq \overline{D}$$

where $D_{N,e}$ is the accumulated damage for the element e, n_e is the total number of elements, $P > 1$, D^{PN} is maximum approximated damage and $\overline{D}$ is the maximum allowable damage.

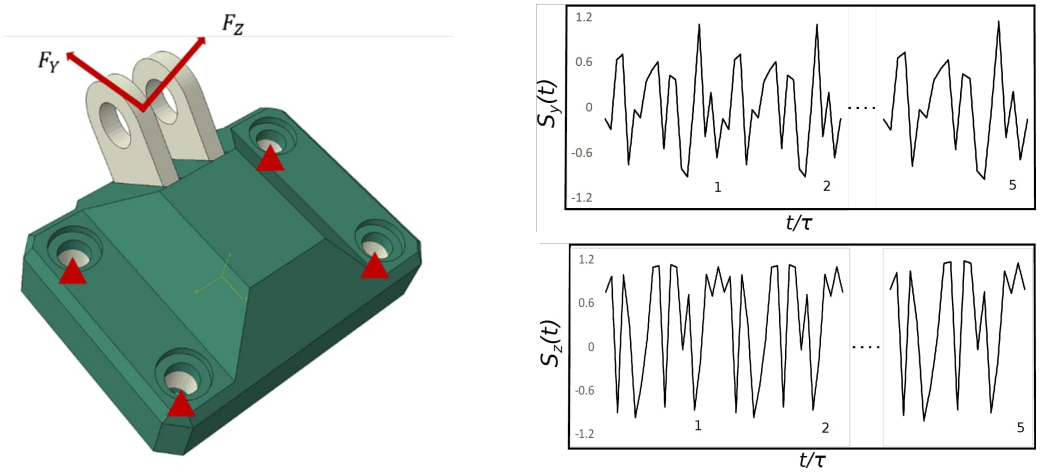

Figure 4.6-1. Geometry of the 3D bracket along with repeats in non-proportional loading spectrum.

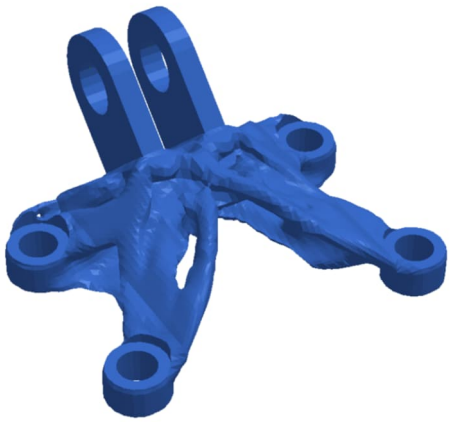

Figure 4.6-2. Optimized result of the 3D bracket with roughly 40% mass reduction.

Using the above definition, the mass minimization problem is

$$(TO)\begin{cases}\min\limits_{x}\sum\limits_{e=1}^{n_e} m_e\rho_e(\boldsymbol{x}) \\ \text{s. t.}\begin{cases}D^{PN}(\boldsymbol{x}) \le \bar{D} \\ \epsilon \le x_e \le 1\end{cases}\end{cases}$$

where m_e is the mass of the element.

As an example, the 3D bracket from Fig. 4.6-1 is tested using the above optimization problem. To the bracket, we apply non-proportional loads in the form $F_y(t) = F_y S_y(t)$ and $F_z(t) = F_z S_z(t)$. Here, $S_y(t)$ and $S_z(t)$ are pseudo-random functions, which are linear interpolation between 20 normally randomized values and these sequences are repeated until $T = t_N = 2E6$ periods. Figure 4.6-2 provides the optimization result of the 3D bracket when subjected to repeats of non-proportional, loading spectrum.

Furthermore, an extension is done in topology optimization [5] that incorporates transversely isotropic material properties into both the constitutive model and the fatigue model.

The work was performed within the Centre for Additive Manufacturing-Metal (CAM^2) financed by Sweden's Innovation Agency under grant agreement No 2016-05175. S. B. Lindström works within the research profile Neopulp financed by the Knowledge foundation. S. B. Lindström thanks Svenska Cellulosa AB (SCA) for financial support.

References

[1] N. S. Ottosen, R. Stenström, and M. Ristinmaa. Continuum approach to high-cycle fatigue modeling. International Journal of Fatigue, 30(6):996–1006, 2008.

[2] S. B. Lindström, J. Moverare, D. Leidermark, H. Ansell, Z. Kapidzic. Incremental fatigue damage modeling of 7050-T7 aluminum alloy at stress-raisers. International Journal of Fatigue, 161 (2022) 106878.

[3] S. Suresh. Topology optimization using a continuous-time high-cycle fatigue model. Structural and Multidisciplinary Optimization, 61, pages 1011–1025, 2020.

[4] S. Suresh. Acceleration of continuous-time, high-cycle fatigue constrained problems in topology optimization. European Journal of Mechanics - A/Solids, 104723, 2022.

[5] S. Suresh. Topology optimization for transversely isotropic materials with high-cycle fatigue as a constraint. Structural and Multidisciplinary Optimization, 63, pages 161–172, 2021.

5 MATERIAL TESTING

5.1 Surface retention of aerostructures

S. Stekovic[1], *L. Selegård*[2] *and NewSoTech*[3]

[1]Engineering Materials, Linköping University, Linköping, Sweden,
[2]Saab Aeronautics, Linköping, Sweden,
[3]NewSoTech AB, Mora

Background

This project has been evaluating the potential of reducing weight of aero components in demanding applications by as much as 40 % by substituting hard chrome on steel with a new nitriding hardening process. Saab Aerostructures aims to reduce fuel consumption of aircraft and implement green alternatives to hard chrome, which was recently banned in the EU. The project will compare the nitriding with hard chrome on steel by materials testing at Linköping University following standards of the aircraft industry. NewSoTech has treated titanium components with their proprietary process technology and adapted and optimized the processes to Saab's requirements. Untreated and treated specimens have been produced and tested at Linköping University in laboratory air. The tests covered hardness, tensile strength and high cycle fatigue. If the results of the evaluation are promising, a business plan will be drafted for the continued commercialization process toward materials qualification.

Fatigue tests

Nitriding is a surface hardening process that is being investigated as a replacement for hexavalent chromium plating of metal components used in aerospace, due to the latter being heavily regulated due to its numerous dangerous health risks [1]. The main aim of this study is to evaluate the effect of two nitriding heat treatments on high cycle fatigue of Ti64 (Grade 5) alloy. For this, axial fatigue tests have been performed on untreated and nitrided round bar specimens under constant amplitude load-controlled mode at a frequency of 20 Hz at ambient conditions. The load ratio was R=0.1. After the testing, the fractured surfaces and microstructures were investigated by scanning electron microscopy (SEM) and cross sections were prepared by focused ion beam (FIB) suitable for SEM and transmission electron microscopy (TEM) analysis.

Cross-sectional analysis show that two different layers were formed after the nitriding processes, namely, a top compound layer and a diffusion layer below it. Non-homogeneities observed in the cross-sections as the thickness varied in both the compound and diffusion layers. The surface roughness parameters also change. It seems that the nitrided layers were influenced by both the microstructure of the base alloy and the surface finish of the specimens. The fatigue results show that the nitriding processes are detrimental to the fatigue life when compared to the extruded Ti64 alloy. However, at a high applied max stress of 850 MPa, the 2nd nitriding process improved the fatigue life. Cracks are initiated from the surface in all nitrided specimens. Transgranular brittle fracture of the nitrided layer was observed in Figure 5.1-1a. A microcrack was found to initiate at a "valley" which then propagates into the base material, Figure 5.1-1b. The nitrided layers experienced cracking when the underlying alloy deformed due to fatigue damage.

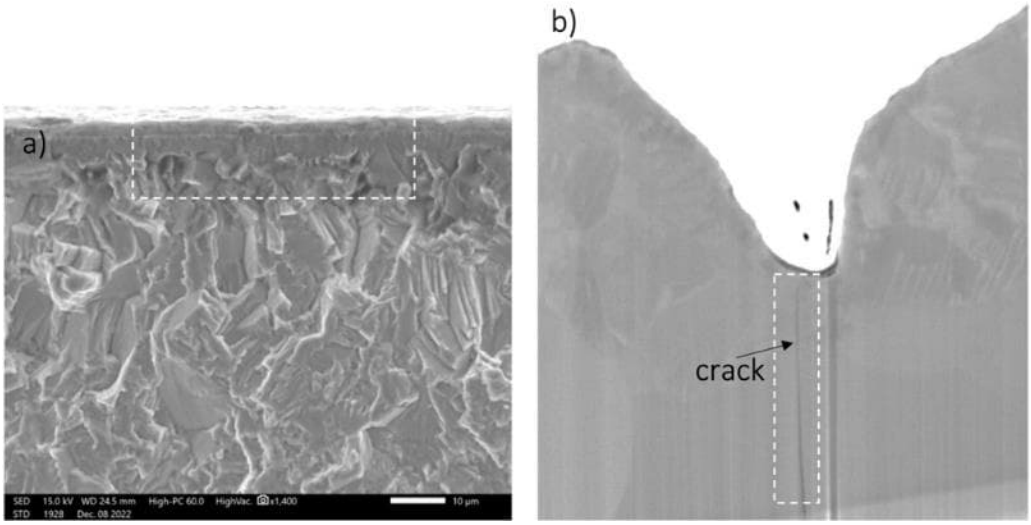

Figure 5.1-1. A fatigue crack initiation site of a specimen treated with a 2nd nitrided process and tested at 800MPa (a) and a cross-sectional view of a crack initiated and propagated from a “valley” (b).

EDS-STEM revealed a very thin (20nm) Al rich layer at the surface, which was not expected, Figure 5.1-2. The layer beneath it consists of TiN while the diffusion layer is a mix of Ti_2N or Ti_2N-Ti mix and the bulk Ti.

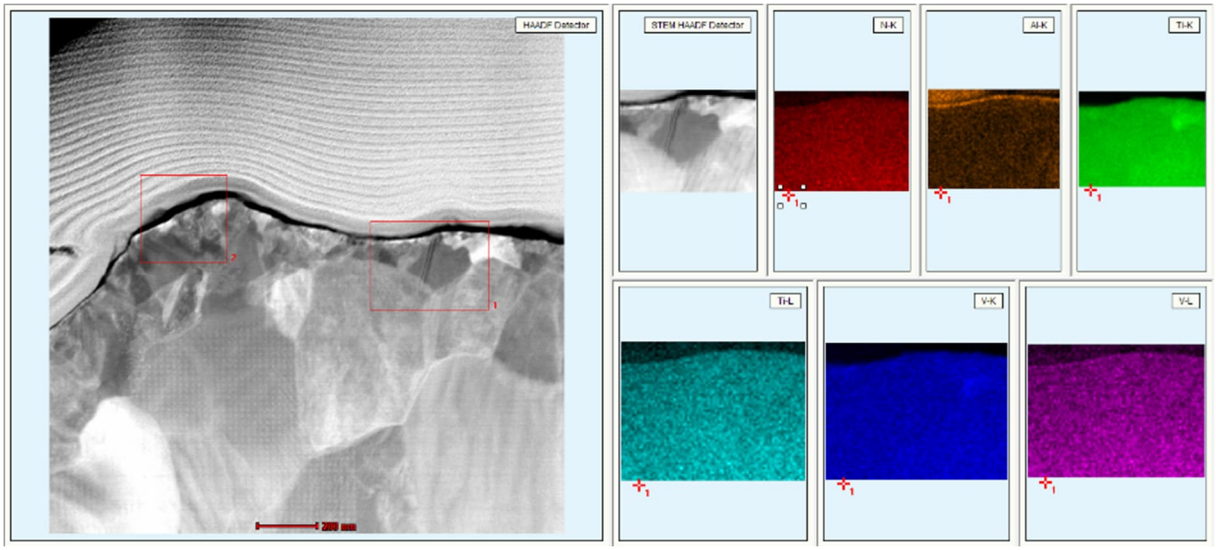

Figure 5.1-2. EDS-STEM of top of the sample shown in Figure 1b.

Further examinations are on-going.

The project is funded by the LIGHTer-programme, reference number 2018-02830.

References

[1] https://echa.europa.eu/regulations/reach/understanding-reach

6 ACKNOWLEDGEMENTS

This editorial work was supported by Saab AB. The editor is also indebted to the following individuals who helped to write this review:

Hennes Wemming	Saab AB/LiU
Jan-Erik Lindbäck	Saab AB
Rikard Rentmeester	Saab AB
Elena Fernandez Rodriguez	Saab AB
Linnea Selegård	Saab AB
Risto Laakso	VTT
Stefan B. Lindström	MittU
Börje Andersson	BARE AB
Robert Pilarczyk	Hill Engineering
Jesse Guymon	Hill Engineering
Svjetlana Stekovic	LiU
Shyam Suresh	LiU
Carl-Johan Thore	LiU
Anders Klarbring	LiU